Inhibition of *O*-GlcNAc transferase activates type I interferon-dependent antitumor immunity by bridging cGAS-STING pathway

Jianwen Chen[1,2,8], Bao Zhao[1,2,8], Hong Dong[1,8], Tianliang Li[1], Xiang Cheng[1,2], Wang Gong[3], Jing Wang[2,4], Junran Zhang[2,5], Gang Xin[1,2], Yanbao Yu[6], Yu L. Lei[3], Jennifer D. Black[7], Zihai Li[2], and Haitao Wen[1,2,9]*

[1]Department of Microbial Infection and Immunity, Infectious Disease Institute, The Ohio State University, Columbus, OH 43210, USA
[2]Pelotonia Institute for Immuno-Oncology, The Ohio State University Comprehensive Cancer Center, The Ohio State University, Columbus, OH 43210, USA
[3]Department of Periodontics and Oral Medicine, University of Michigan School of Dentistry, University of Michigan Rogel Cancer Center, University of Michigan, Ann Arbor, MI 48105, USA
[4]Department of Cancer Biology and Genetics, The Ohio State University, Columbus, OH 43210, USA
[5]Department of Radiation Oncology, The Ohio State University, Columbus, OH 43210, USA
[6]Department of Chemistry and Biochemistry, University of Delaware, Newark, DE 19716, USA
[7]Eppley Institute for Research in Cancer and Allied Diseases, University of Nebraska Medical Center, Omaha, NE 68198, USA
[8]These authors contributed equally to this work.
[9]Lead Contact

*Correspondence: Dr. Haitao Wen, email: Haitao.Wen@osumc.edu
Telephone: 614-292-6724, Fax: 614-292-9616
Address: 796 Biomedical Research Tower, 460 W 12th Ave, Columbus, OH 43210

Abstract

The *O*-GlcNAc transferase (OGT) is an essential enzyme that mediates protein *O*-GlcNAcylation, a unique form of posttranslational modification of many nuclear and cytosolic proteins. Recent studies observed increased OGT and *O*-GlcNAcylation levels in a broad range of human cancer tissues compared to adjacent normal tissues, indicating a universal effect of OGT in promoting tumorigenesis. Here, we show that OGT is essential for tumor growth in immunocompetent hosts by repressing the cyclic GMP-AMP synthase (cGAS)-dependent DNA sensing pathway. We found that deletion of OGT ($Ogt^{-/-}$) caused a marked reduction in tumor growth in both syngeneic tumor models and a genetic colorectal cancer (CRC) model induced by mutation of the *Apc* gene (Apc^{min}). Pharmacological inhibition or genetic deletion of OGT induced a robust genomic instability (GIN), leading to cGAS-dependent production of the type I interferon (IFN-I) and IFN-stimulated genes (ISGs). As a result, deletion of *Cgas* or *Sting* from $Ogt^{-/-}$ cancer cells restored tumor growth, and this correlated with impaired $CD8^+$ T cell-mediated antitumor immunity. Mechanistically, we found that OGT-dependent cleavage of host cell factor C1 (HCF-1) is required for the avoidance of GIN and IFN-I production in tumors. In summary, our results identify OGT-mediated genomic stability and activate cGAS-STING pathway as an important tumor cell-intrinsic mechanism to repress antitumor immunity.

Introduction

Cancer cells can maintain malignant phenotypes partially due to altering the post-translational modification (PTM) patterns of cancer-related functional proteins under the stimulation of extracellular and intracellular factors [1]. Protein modification by the *O*-linked β-N-acetylglucosamine (*O*-GlcNAc) is a dynamic and reversible post-translational modification, which is added to the hydroxyl group of a specific serine or threonine residue in a target protein by *O*-GlcNAc transferase (OGT) and removed by *O*-GlcNAcase (OGA) [2]. *O*-GlcNAcylation is a fast-cycle and nutrient-sensitive PTM, which modifies thousands of cytoplasmic, nuclear, and mitochondrial proteins and mediates crosstalk with protein phosphorylation, regulating signal transduction and affecting protein localization, activity, stability, and protein-protein interaction. Dysregulation of *O*-GlcNAcylation is associated with multiple metabolic diseases and cancer [3, 4].

Recent studies observed increased OGT and *O*-GlcNAcylation level in human colon cancer tissues compared to adjacent normal tissues [5-7], indicating an essential role of OGT-mediated protein *O*-GlcNAcylation in the pathogenesis of colon cancer. Several oncogenic proteins that are involved in the pathogenesis of colon cancer have been shown to be directly modified by *O*-GlcNAc, including β-catenin and NF-κB [8-10]. For example, *O*-GlcNAcylation of β-catenin at T41 inhibits its phosphorylation, which subsequently attenuates its ubiquitination and degradation and promotes oncogenic activity [7, 11]. In contrast, inhibitory roles of *O*-GlcNAc signaling in the growth of human colon cancer and in oncogenic Wnt/β-catenin signaling have also been reported [12, 13]. The aforementioned studies show that *O*-GlcNAc modification of specific proteins can play opposing roles in tumorigenesis. However, the overall effect of OGT-mediated *O*-GlcNAcylation in cancer remains unknown.

The cGAS/STING cytosolic DNA-sensing pathway plays a vital role in activating the innate immune response and production of the type I interferons (IFN-I) [14]. Cyclic guanosine monophosphate (GMP)–adenosine monophosphate (AMP) synthase (cGAS) interacts with cytosolic double-stranded DNA (dsDNA) in a sequence-independent manner. The direct binding of cGAS to cytosolic dsDNA promotes cGAS homodimerization and activates the catalytic activity of cGAS, producing 2', 3'-cyclic GMP-AMP (cGAMP) from ATP and GTP. The second messenger cGAMP binds to and activates the endoplasmic resident stimulator of interferon genes (STING). Once activated, STING translocates to the ER-Golgi intermediate compartment (ERGIC) to recruit TANK-binding kinase 1 (TBK1) and IFN regulatory factor 3 (IRF3), leading to the production of IFN-I and activation of numerous IFN-stimulated genes (ISGs) [15-17]. However, it remains largely unknown whether OGT expression affects cGAS-STING pathway and antitumor immunity.

In this study, we find that deficiency or pharmacological inhibition of OGT and subsequent accumulation of cytosolic dsDNA activates the cGAS-STING pathway and induces $CD8^+$ T cell-dependent antitumor immunity. Deletion of cGAS or STING diminishes DNA sensing and lead to progressive tumor growth. Mechanistically, we show that OGT could interacts with HCF-1 and cleaves it, which contributes to the maintenance of genomic stability. Re-expression of $HCF\text{-}1^{C600}$ in $Ogt^{-/-}$ tumor cells inhibit production of cytosolic dsDNA and IFN-I. In summary, our findings demonstrate that OGT-mediated DNA damage and activate cGAS-STING pathway as an important tumor cell-intrinsic mechanism to repress antitumor immunity and provides a window for potential therapeutic opportunities for in OGT-dependent cancer.

Results

Increased OGT expression in human and mouse tumor samples

Protein *O*-GlcNAcylation is upregulated in various cancers [12, 18-21]. OGT is the only known enzyme that mediates *O*-GlcNAcylation of proteins at the Ser or Thr residues [22], we hypothesized that OGT could serve as an important regulator to regulate cancer cell growth and serve as a biomarker for cancer. Initial analysis of data from The Cancer Genome Atlas (TCGA) dataset in GEPIA2 (http://gepia2.cancer-pku.cn/#index) and found a significant positive correlation between *OGT* mRNA expression and tumorigenesis in bladder urothelial carcinoma (BLCA), cholangiocarcinoma (CHOL), colon adenocarcinoma (COAD), esophageal carcinoma (ESCA), head and neck squamous cell carcinoma (HNSC), kidney chromophobe (LIHC), lung adenocarcinoma (LUAD), prostate adenocarcinoma (PRAD), rectum adenocarcinoma (READ), sarcoma (SARC), and a stomach adenocarcinoma (STAD) (Supplemental Fig. 1A). Next, we utilized UALCAN database analysis, and found that *OGT* mRNA expression was compared between 286 COAD samples and 41 adjacent or normal samples, the expression of *OGT* was significantly increased in COAD at the transcriptional level (Fig. 1A). A significant positive correlation tendency between *OGT* mRNA expression and individual different tumor stages was observed. The stage IV COAD tissues exhibited the highest expression level of *OGT* in compared with low stage (Fig. 1B). We also observed a significant positive correlation between *OGT* mRNA expression and nodal metastasis status (Fig. 1C). Furthermore, we found that the protein level of OGT was also significantly increased in COAD patient samples and amongst individual different stages based on the CPTAC and HPA online database (Fig. 1D-F). Similar results are found in LUAD (Supplemental Fig. 1B-F). These results suggest that high mRNA and protein levels of OGT in tumorigenesis were consistent in different databases.

To determine whether intestinal OGT expression was increased in *Apc*^{min} colorectal tumor mouse model, intestinal tissues were collected for western blot and immunohistochemical staining (IHC) analysis. Intestinal OGT protein was markedly increased in *Apc*^{min} mouse tumor tissues compared to adjacent or normal tissues (Fig. 1G). As expected, *O*-GlcNAcylation proteins levels in intestinal tissues were also significantly higher in tumor tissues than adjacent or normal tissues. IHC staining revealed that mouse OGT protein was markedly higher in tumor tissues than in adjacent tissues (Fig. 1H), which was consistent with the expression pattern in human samples. OGT protein was also upregulated in the azoxymethane (AOM)/dextran sodium sulfate (DSS) colorectal tumor model (Fig. 1I-K). Together, these data strongly suggest that OGT may play a critical role in tumorigenesis and serve as a prognostic marker and therapeutic target in cancer treatment.

Epithelial OGT deletion inhibits mouse colorectal tumorigenesis

To determine whether OGT may be an important therapeutic target for tumor treatment, we generated an intestinal epithelial cell-specific *Ogt* deletion (*Ogt*$^{\Delta IEC}$) by crossing *Ogt*$^{fl/fl}$ mice with Villin-Cre mice. *Ogt*$^{\Delta IEC}$ mice were then crossed with *Apc*^{min} mice to generate *Ogt*$^{\Delta IEC}$*Apc*^{min} mice (Supplemental Fig. 2). To determine whether intestinal OGT expression was decreased in *Ogt*$^{\Delta IEC}$*Apc*^{min} mice, intestinal tissues were collected for western blot analysis. Intestinal OGT levels were drastically decreased in *Ogt*$^{\Delta IEC}$*Apc*^{min} mice compared to wildtype *Apc*^{min} mice (Fig. 2A). Importantly, deletion of the *Ogt* in intestinal epithelial cells resulted in significantly reduced tumor size and total number of polyps at 20 weeks of age (Fig. 2A), indicating that OGT promotes oncogenic transformation in colorectal tumor *in vivo*. To gain insight into the role of protein on intestinal carcinogenesis in intestinal cancer, we examined the differences in intestinal

carcinogenesis. Hematoxylin and eosin (H&E) staining demonstrated that epithelial inflammation increased in *Ogt*$^{\Delta IEC}$*Apc*^{min} mice compared to wildtype *Apc*^{min} mice (Fig. 2B). OGT deficiency in intestinal tissues was also associated with significantly elevated gene expression of key pro-inflammatory cytokines like interleukin *Il1α*, *Il6*, *TNF-α*, as well as several interferons and ISGs like *Isg15*, *Mx1*, *Cxcl10* (Fig. 2C). Furthermore, we found IL-2, IL-6, IL-10, IL-17, IFN-α, IFN-β, IFN-γ and CXCL10 were upregulated compared with control mice (Fig. 2D).

OGT deficiency activates cGAS/STING-dependent IFN-I pathway

Based on previous studies, we found that several interferons and several interferon-stimulated genes, such as *Isg15*, *Mx1*, IFN-α, IFN-β and *Cxcl10* were upregulated. We hypothesized that OGT deficiency may activate the type I IFN pathway. First, we generated *Ogt* knock outs of murine colorectal carcinoma models like MC38, LLC, B16-OVA and of a human colorectal cell line, HT29. We then evaluated the expression changes of *Ifna4*, *Ifnb1*, *Isg15*, *Mx1* and found that all the genes except *Ifna4* mRNA expression were significantly increased in all cultured *Ogt* knockout cells (Fig. 3A-D). Next, we investigated how the type I IFN pathway in *Ogt* knockout cells was activated [23, 24]. We found that while the phosphorylation of STAT1, TBK1 and IRF3 is increased, the STING expression is reduced in *Ogt* knockout MC38, LLC, B16-OVA and HT29 cells (Fig. 3E-F). To determine whether this effect is specific for *Ogt* knockout, we stably expressed exogenous OGT in *Ogt* knockout cells and found that the type I IFN pathway activation effect is abolished (Fig. 3F). The type I IFN pathway is typically activated by both viral RNA and dsDNA. In order to eliminate the type I IFN pathway activate independent on RNA but dependent on dsDNA, we knocked out MAVS protein in *Ogt*$^{-/-}$ cells, which is a RNA pivotal adaptor protein activate the downstream protein kinase TBK1, IFN pathway and ISGs in *Ogt*$^{-/-}$ cells (*24*), and we

found that knockout of MAVS in *Ogt*$^{-/-}$ cells has no effect on either *Isg15*, *Mx1*, *Ifna4* and *Ifnb1* expression or the type I IFN pathway (Fig. 3G-H).

We further investigated the mechanism of the type I IFN signaling activation and found that *Ogt* knockout induced the reduction of the STING. This result is similar to previous studies [25, 26]. The phenotype of *Ogt* knockout implies that STING is involved in the activation of the type I IFN pathway. We hypothesized that OGT negatively regulates type I IFN through the cGAS/STING pathway. Next, we produced the OGT/cGAS and OGT/STING double knockout cells both in MC38, HT29 and B16-OVA. Surprisingly, these type I IFN and *Cxcl10* signals disappeared in OGT/cGAS and OGT/STING double knockout cells both in mRNA and protein level (Fig. 3I-L).

The type I IFN signaling is a key pathway that promotes antigen presentation and DC activation [27-29]. Phagocytosis of extracellular tumor DNA by DCs triggers the activation of the cGAS-STING-IFN pathway [30, 31]. To determine whether the increased cGAS-STING-IFN signaling in *Ogt* knockout cells provides an activated signal for single epitope-specific CD8$^+$ T cell priming by antigen-presenting cells (APCs), we added the supernatant from B16-OVA tumor cells into the co-culture system of BMDCs and OT-I cells. The results showed that BMDCs pre-cultured with *Ogt*$^{+/+}$ or *Ogt*$^{-/-}$ B16-OVA tumor cells supernatant provided a potent activated signal for optimal single epitope-specific T cell proliferation (Fig. 3M), while cGAS or STING deficiency in *Ogt*$^{-/-}$ tumor cells diminished such effects (Fig. 3N). Further, we added the supernatant from *Ogt*$^{+/+}$ or *Ogt*$^{-/-}$ B16-OVA tumor cells into the co-culture system of *Ifnar1* knockout BMDCs and OT-I cells. The cell proliferation was abolished when treated with *Ifnar1*$^{-/-}$ BMDCs pre-cultured with *Ogt*$^{+/+}$ or *Ogt*$^{-/-}$ B16-OVA tumor cells supernatant. (Supplemental Fig. 3). These results demonstrated that *Ogt* deficiency activate antitumor CD8$^+$ T cells response is dependent on the

type I IFN signal in dendritic cells and in a manner dependent on the tumor-cell-intrinsic cGAS-STING pathway.

OGT deficiency causes DNA damage and cytosolic DNA accumulation

Because the accumulation of cytosolic DNA is a consequence of nuclear DNA damage, which can activate immune response. The cGAS senses cytoplasmic DNA as a consequence of nuclear DNA damage [32]. Previous studies showed that the STING is degraded while cGAS-STING is activated [25]. As mentioned above, the STING degraded in *Ogt* knockout cells. We hypothesized that whether the cytosolic DNA is accumulated in *Ogt* knockout cells, we stained cytosolic double-strand DNA (dsDNA) with PicoGreen, a widely used immunofluorescence staining that selectively binds to dsDNA [33, 34], and found that a significantly higher percentage of *Ogt* deficiency cells than control cells in two different *Ogt* knockout MC38 and LLC cell clones, respectively (Fig. 4A and Supplemental Fig. 4A). In addition, we also stained dsDNA with anti-dsDNA immunofluorescence and the results were similar to PicoGreen staining (Fig. 4B and Supplemental Fig. 4B). We next assessed the phosphorylation of H2AX at Ser 139 (γH2AX), an indirect marker of DNA DSBs in the cell lines [35]. Comparable expression levels of H2AX, we found that γH2AX was dramatically increased in *Ogt* knockout MC38, LLC, HT29 and B16-OVA cells (Fig. 4C and 4F). We also used the anti-γH2AX immunofluorescence staining and comet assays, a classical quantifying and analyzing DNA damage, and found that *Ogt* knockout significantly induced immense DNA strand breakage in MC38 cells (Fig. 4D-E). Finally, the rescued results showed that exogenous OGT expression abolished the γH2AX expression both in MC38, LLC, HT29 and B16-OVA cells and DNA damage in MC38 cells (Fig. 4F-H). Together, these data indicated that *Ogt* knockout caused DNA damage and induced the cytosolic DNA accumulation.

The C-terminus of HCF-1 rescues DNA damage and IFN-I pathway in *Ogt*$^{-/-}$ cells

Previous studies in Fig. 3F and Fig. 4F showed that expression of exogenous OGT abolished the type I IFN and γH2AX signals. To explore the mechanism how OGT regulate the IFN and γH2AX production. Next, we use GFP agarose immunoprecipitation and liquid chromatography coupled to tandem MS (LC-MS/MS) to identify different proteins that interacted with OGT in human colonic cancer cell line HT29. Interestingly, HCF-1 was the most enriched protein in the precipitates from *OGT* restored HT29 knockout cells compared to *OGT* knockout cells reconstituted with empty vector, based on the number of peptides (indicating the identification confidence) and the number of peptide-spectrum matches (PSMs, indicating the abundance) (Fig. 5A and Supplemental Table 4). Previous studies showed that the human epigenetic cell-cycle regulator (HCF-1) undergoes an unusual proteolytic maturation by OGT cleavage and process resulting in stably associated HCF-1^{N1011} and HCF-1^{C600} subunits that regulate different aspects of the cell cycle [36]. We found similar results in this study by using co-immunoprecipitation assay (Fig. 5B-C). We rescued the HCF-1 cleavage phenotype by expression of exogenous OGT (Fig. 5D). To clarify how to OGT regulate function of HCF-1, we transfected empty vector (EV), the full-length HCF-1-HA (HCF-1^{FL}), HCF-1$^{1-1011}$-HA (HCF-1^{N1011}), HCF-1$^{1-450}$-HA (HCF-1^{N450}), HCF-1$^{450-1011}$-HA (HCF-1$^{N450-1011}$) and HCF-1$^{1436-2035}$-HA (HCF-1^{C600}) and myc-OGT and found that OGT can bind HCF-1^{C600} (Fig. 5E), furthermore OGT directly bind the HCF-1^{C600} (Supplemental Fig. 5A-B). To further understand the physiological function of HCF-1, we transfected EV, HCF-1^{FL}, HCF-1^{N1011}and HCF-1^{C600} into MC38 control and OGT knockout cells, respectively. As shown in Fig. 5F, transfected HCF-1^{FL} and HCF-1^{N1011} didn't rescue the gene expression differences, such as *Isg15*, *Mx1* and *Ifnb1*, but HCF-1^{C600} can restore the gene expression differences. These results were confirmed by using western blot and anti-dsDNA

immunofluorescence staining (Fig. 5G-H). Overall, these data indicated that OGT regulates the HCF-1 cleavage and maturation, HCF-1^{C600} can eliminate the cytosolic DNA accumulation, DNA damage, the type I IFN activation and restrain cGAS-STING-mediated DNA sensing.

OGT deficiency inhibits tumor progression through enhancing infiltration by CD8$^+$ T cells

We examined whether inhibiting *Ogt* can delay the tumor growth and prolong the survival. To further verify these effects, we utilized transplanted tumor model. We found that the *Ogt* deficiency MC38 colorectal tumor cells have no obvious inhibit cell growth *in vitro* (Supplemental Fig. 6A). However, we found that a significant delay in tumor growth, tumor weight and prolong mice survival compared to the control group (Fig. 6A-B). We also used lewis lung carcinoma (LLC) cells and the B16-OVA melanoma cells because they represent an aggressive murine tumor model and are highly resistant to various immunotherapies, similar results were shown in Fig. 6C-D and Supplemental Fig. 6B-E. These results showed that *Ogt* deficiency could delay tumor growth and prolong survival of mice in MC38, LLC, and B16-OVA tumor model. We next examined whether the enhanced antitumor function is related to tumor microenvironment (TME). Consistently, tumors from C57BL/6 immunocompetent mice bearing *Ogt*$^{-/-}$ MC38 tumors compared with MC38 control tumors, showed higher proportion of CD8$^+$ and CD4$^+$ T cells, functional CD8$^+$ IFN-γ$^+$, CD8$^+$ TNF-α$^+$ and CD8$^+$ IFN-γ$^+$ TNF-α$^+$ double positive T cells, but not CD45$^+$, CD11b$^+$ CD11c$^+$, CD11b$^+$ F4/80$^+$, CD11b$^+$ Ly6C$^+$ and Treg cells (Fig. 6E-H and Supplemental Fig. 7D-H). The similar results were also observed in mice challenged with LLC or B16-OVA cells (Supplemental Fig. 7I-P).

To determine whether *Ogt* deficiency is dependent upon adaptive immune system, we inoculated MC38 control and *Ogt* knockout cells into immunodeficient *Rag2*$^{-/-}$ mice and tracked tumor growth. The difference of tumor growth rate disappeared between MC38-*Ogt* knockout and

control ones (Fig. 6I), indicating their association with an impaired immune response. We then postulated that *Ogt* knockout might have potent antitumor effects *in vivo* through $CD4^+$ T and $CD8^+$ T cells. In order to test this hypothesis, we performed antibody-mediated $CD4^+$ T or $CD8^+$ T cells depletion in $Ogt^{-/-}$ and control tumor-bearing mice and examined the tumor growth and survival. Depletion $CD8^+$ T cells dramatically enhanced the tumor growth in $Ogt^{-/-}$ tumor-bearing mice, compared to the isotype antibody treatment group, and their antitumor activity of *Ogt* deficiency disappeared, both in tumor volume, weight and survival curve (Fig. 6J-K). However, depletion $CD4^+$ T cells have no obvious effect both in tumor volume and weight in $Ogt^{-/-}$ tumor-bearing mice, compared to the isotype antibody treatment group (Supplemental Fig. 8A). These results implied that $CD8^+$ T cells mediated the inhibitory effect of *Ogt* deficiency on tumor progression.

Next, to determine whether this effect is specific for OGT knockout, we performed this experiment *in vivo* using MC38 tumor-bearing rescue model. As we expected, decreased tumor growth and prolong mice survival phenotype disappeared both in OGT rescued cells (Fig. 6L-M) and in OGT/cGAS or OGT/STING double knockout tumors (Fig. 6N-O). Furthermore, flow cytometry results showed that the proportion of $CD4^+$ T and $CD8^+$ T cells, $CD8^+$ IFN-γ^+ and $CD8^+$ TNF-α^+ disappeared both in OGT rescued cells (Supplemental Fig. 8B-D) and in OGT/cGAS or OGT/STING double knockout tumors *in vivo* (Fig. 6P and Supplemental Fig. 8E-F). These results proved that OGT deficiency induces the cGAS/STING and activates the type I IFN pathway.

Increasing evidences support that intratumoral infiltration of $CD8^+$ T cells dictates the response to immune checkpoint blockade (ICB) therapy and its efficacy on various cancers [37, 38]. Blocking PD-L1 can restore the anti-tumor immune function and enhance the antitumor immunity by promoting CD8-positive T-cell infiltration, which is widely used in clinical

immunotherapy [39, 40]. Because *Ogt* deficiency induced tumor cell-intrinsic immune response to recruit $CD8^+$ T cells into MC38, LLC and B16-OVA cells, we hypothesized that *Ogt* deficiency potentiated enhance the efficacy of PD-L1 blockade *in vivo*. To test this hypothesis, we carried out the combination treatment of *Ogt* knockout and neutralizing antibody (anti-PD-L1). MC38 and LLC tumor growth was significantly delayed in tumor-bearing mice treated with PD-L1 antibody compared to isotype control (Fig. 6Q and Supplemental Fig. 8G), which translated into extended survival (Fig. 6R and Supplemental Fig. 8H). Deletion of *Ogt* synergized with PD-L1 blockade treatments to improve antitumor immunity. We next assessed the potential relevance of *OGT* in human cancer immunity. We first analyzed gene expression profiles of cancer patients from TCGA database and survival, we found that low *OGT* expression was associated with improved overall survival (OS) and progression free survival (PFS) in patients with COAD (Fig. 6S-T). Using TIMER2.0 (http://timer.cistrome.org) analysis, we found that *OGT* expression negatively correlated with $CD8^+$ T cell infiltration (Fig. 6U). For further analysis, we found that a set of genes associated with immune response was robustly regulated in *OGT* high and *OGT* low patients. The response interferon-gamma, interferon-gamma production, cellular defense response, regulation of inflammatory response, acute inflammatory response is upregulated; DNA mismatch repair is a downregulated processe, as shown by Gene Ontology (GO) enrichment and pathway analysis (Supplemental Fig. 9A). Gene Set Enrichment Analysis (GSEA) showed that T cell activation, response to interferon-gamma, interferon-gamma production, antigen processing and presentation, interleukin-1/12 production, dectin-1 mediated noncanonical NF-κB signaling are negatively correlated with *OGT* expression (Supplemental Fig. 9B-H), while mismatch repair, covalent chromatin modification and DNA repair complex are positively correlated with *OGT* expression (Supplemental Fig. 9I-K). Of our most interest, we found that *CD8A*, *IFNG*, *ISG15*, *MX1*, *CD274*

and *CXCL10* expression are negatively correlated with *OGT* expression (Supplemental Fig. 9L-Q). These data suggest a potential involvement of *OGT* deficiency and antitumor immunity in patients with cancer.

Combination therapy with OSMI-1 and anti-PD-L1 Ab augmented T cells and antitumor immunity

Based on previous studies, we know that *Ogt* knockout causes DNA damage, accumulates cytosolic DNA, induces cGAS-STING pathway and activates antitumor immunity. Here we speculated that OGT inhibitor may cause DNA damage and activate antitumor immunity. OSMI-1 is a small molecule inhibitor of OGT that does not significantly affect other glycosyltransferases and is active in a very low doses [41]. The cell proliferation exhibited no obvious difference in different concentrations in MC38 and LLC cells *in vitro* assay (Supplemental Fig. 10A-B). We stained cytosolic dsDNA with anti-dsDNA and found that treatment with OSMI-1 could significantly induce a high percentage of cytosolic DNA accumulation (Fig. 7A and Supplemental Fig. 10C). We next examined the DNA damage and found that γH2AX was obviously increased in OSMI-1 treated cells (Fig. 7B-C). We also performed the anti-γH2AX immunofluorescence staining and found that OSMI-1 significantly induced immense DNA strand breakage in treated cells (Fig. 7D and Supplemental Fig. 10D).

As we all know, the presence of cytosolic DNA could trigger activation of cGAS-STING pathway [42]. To investigate whether OSMI-1 activated cGAS/STING pathway, we examined activation of major regulators of the pathway in OSMI-1-treated MC38 and LLC cells, as indicated by increased phosphorylation of STAT1, TBK1, and IRF3 and reduced STING expression (Fig.7B-C), which is consistent with *Ogt* knockout cells. As mentioned earlier, deletion of *Ogt* synergized with PD-L1 blockade treatments to improve antitumor immunity. We next sought to

322 determine whether OSMI-1 enhanced the antitumor immune effect of anti-PD-L1 antibody *in vivo*
323 by using MC38 tumor-bearing model. To our surprise, similar to anti-PD-L1 therapy, OSMI-1
324 alone significantly inhibited MC38 tumor growth and survival, and the combination of OSMI-1
325 and anti-PD-L1 therapy resulted in superior tumor suppression compared with monotherapy (Fig.
326 7E-F). Flow cytometry results showed that proportion of $CD4^+$ T and $CD8^+$ T cells was increased
327 both in OSMI-1, anti-PD-L1 treatment alone and combined treatment with OSMI-1 and anti-PD-
328 L1 antibody (Fig. 7I), production of IFN-γ and TNF-α were significantly enhanced in intratumoral
329 $CD8^+$ T cells not only combined treatment with OSMI-1 and anti-PD-L1 antibody, but also single-
330 agent OSMI-1 treatment (Fig. 7J-K). This pharmacological inhibition model is consistent with
331 MC38 *Ogt* knockout tumor-bearing mice model.

332 Furthermore, we treated mice bearing LLC tumors, because it represents a most aggressive
333 murine tumor model and are highly resistant to various immunotherapies. Our results showed that
334 treatment with single-agent OSMI-1 can slightly inhibited LLC tumor growth and survival.
335 Combined treatment with OSMI-1 and anti-PD-L1 antibody caused significantly greater tumor
336 suppression than either monotherapy (Fig. 7F-G). We also found that proportion of $CD4^+$ T and
337 $CD8^+$ T cells was significantly increased in combined treatment with OSMI-1 and anti-PD-L1
338 antibody. However，single-agent OSMI-1 or anti-PD-L1 antibody treatment cannot significantly
339 increased the proportion of $CD4^+$ T and $CD8^+$ T cells (Fig. 7L). Production of IFN-γ and TNF-α
340 were significantly enhanced in intratumoral $CD8^+$ T cells in combined treatment with OSMI-1 and
341 anti-PD-L1 antibody, but not in single-agent OSMI-1 or anti-PD-L1 treatment (Fig. 7M-N). This
342 model is also consistent with *Ogt* knockout tumor-bearing mice model. In summary, OGT inhibitor
343 OSMI-1 induces DNA damage and cytosolic DNA accumulation, activates cGAS/STING
344 pathway. Combined OGT inhibitor with anti-PD-L1 antibody markedly suppressed tumor growth

and increased $CD8^+$ T cells and production of IFN-γ and TNF-α in tumor. These results demonstrated a pivotal role of OGT inhibition in augmenting the antitumor immune response of ICB. Given the increasing importance of immunotherapy for the management of patients with that OGT inhibitors, combined with anti-PD-L1 blockade may offer a particularly attractive strategy for the treatment of colorectal and lung cancer, which are instrumental in turning ‘cold tumors’ into ‘hot tumors’.

Discussion

As an important metabolic enzyme, OGT promotes tumorigenesis by glycosylating numerous proteins. This study found that OGT levels are elevated in both human and mouse tumors (Fig. 1). Additionally, epithelial deletion of OGT inhibits colorectal tumorigenesis in mice (Fig. 2). DNA damage and DNA repair signaling pathways play pivotal roles in maintaining genomic stability and integrity by correcting impaired DNA, which otherwise can contribute to carcinogenesis [43]. These pathways are activated in response to endogenous or exogenous DNA-damaging agents, helping cells to preserve genomic stability. HCF1 is a member of the host cell factor family, involved in regulating the cell cycle and playing regulatory roles in various transcription-related processes. This study found that OGT deficiency leads to DNA damage and cytosolic DNA accumulation (Fig. 4) by regulating HCF-1 cleavage and maturation (Fig. 5). In antitumor therapies, chemotherapy and radiotherapy induce cell death by directly or indirectly causing DNA damage, thereby increasing tumor sensitivity to cancer therapies. DNA damage-inducing therapies have proven to be immensely beneficial for cancer treatment, functioning by directly or indirectly forming DNA lesions and subsequently inhibiting cellular proliferation. Therefore, targeting DNA repair pathways may represent a promising therapeutic approach for cancer treatment. In this study, we observed that deletion of OGT leads to uncontrolled expansion of DNA damage and induces cytosolic dsDNA accumulation in tumor cells, suggesting that OGT is a promising therapeutic target for cancer treatment.

The cytosolic DNA sensing pathway has emerged as the major link between DNA damage and innate immunity, DNA damage in the nucleus results in the accumulation of cytosolic DNA, which activate the cGAS–STING pathway [44-49]. This study found that OGT deficiency activates the cGAS/STING-dependent IFN-I pathway (Fig. 3), resulting in the expression of proinflammatory

cytokines (e.g., IFNB1 and ISGs) and chemokines (e.g., CXCL10) in a TBK1-IRF3-dependent manner. OGT deficiency causes DNA damage and cytosolic DNA accumulation, which triggers this response. The cGAS–STING pathway is the key cytosolic DNA sensor responsible for the type I IFN production, DC activation, and subsequent priming of $CD8^+$ T cells against tumor-associated antigens [30, 50, 51]. Recent evidence shows that proper activation of tumor cell-intrinsic immunity or innate immune cells can enhance antitumor immunity [34, 52, 53]. In this study, cGAS-STING-IIFNB1-CXCLl10 signaling axis can provide an activated signal for epitope-specific $CD8^+$ T cell priming by antigen-presenting cells. Ultimately, this process results in increased infiltration of tumor-infiltrating CD8+ T lymphocytes and more effective inhibition of tumor growth within the tumor microenvironment (TME) (Fig 6). However, knockout of cGAS or STING can eliminate the proliferation signal of CD8+ T cells and abolish antitumor immunity (Supplemental Fig. 11).

Immunotherapy with checkpoint-blocking antibodies targeting CTLA-4 and PD-1/PD-L1 has revolutionized cancer treatment and drastically improved the survival of individuals in the clinical treatment. Although immunotherapy has made great progress in the treatment of solid tumors, only around 20% of patients with non-small cell lung cancer (NSCLC) respond to mono-immunotherapy, and a large proportion of individuals develop resistance. Therefore, there is a need to explore novel alternative strategies and personalized immunotherapy strategies through combinations of PD-1/PD-L1 blockade with small molecular targets. This is aimed at improving sensitivity to activated antitumor immune responses in patients and addressing drug resistance [54, 55]. Here we showed that the OGT inhibitor OSMI-1 induced DNA damage and cytosolic DNA accumulation which led to activation of the cGAS-STING-TBK1-IRF3 pathway, then enhanced the innate and adaptive immune responses to tumor cells, which reversed the immunosuppressive

399 TME by increasing $CD8^+$ T cells infiltration. To our surprise, especially in lung cancer mice model,
400 combination therapy with OSMI-1/PD-L1 can achieve a better antitumor effect than either
401 monotherapy (Fig7).

402 In summary, our findings demonstrated deficiency in OGT mediated genomic instability
403 and result in cytosolic dsDNA accumulation, which activating the cGAS-STING signaling
404 pathway, increasing inflammatory cytokines, and enhancing antitumor immunity. Our study also
405 addresses an unmet clinical need through the combination of OGT inhibition and anti-PD-L1
406 therapy, which may represent a promising strategy for colorectal and lung cancer therapy.
407

Acknowledgments

We thank members of the Wen lab for discussion. This work was supported by National Institutes of Health (NIH) grants R01GM135234 and R01AI162779 (H.W.), R01AI077283 and R01CA262089 (Z.L.), R01DE026728 (Y.L.) and The Ohio State University Comprehensive Cancer Center Intramural Research Program (A.M., D.M.J., K.H. and H.W.).

Conflict of Interest

The authors declare no competing interests.

Declarations

Ethics approval and consent to participate The National Institutes of Health Guide for the Care and Use of Laboratory Animals was followed in this study. The study was approved by the Ethics Committee of The Ohio State University and all procedures were conducted in accordance with the experimental animal guidelines of The Ohio State University (Project ID 2018A00000022).

Materials and methods

Mice

Ogt$^{\Delta IEC}$*Apc*^{min} mice were generated by crossing the *Ogt*$^{fl/fl}$ mice with Villin-Cre mice, then crossed with *Apc*^{min} mice. C57BL/6 mice, *Apc*^{min} mice, Villin-Cre mice, *Rag2*$^{-/-}$ mice, *Ifnar1*$^{-/-}$ mice and OT-I mice were purchased from Jackson Laboratories. Mice between 8 to10 weeks of age were used for the animal experiments, tail genomic DNA was isolated for genotyping. Primers for genotyping PCR are listed in Supplemental Table 1. All *in vivo* experiments were conducted in accordance with the National Institutes of Health Guide for the Care and Use of Laboratory Animals and the Institutional Animal Care and Use Committee. The study was approved by the Ethics Committee of The Ohio State University and all procedures were conducted in accordance with the experimental animal guidelines of The Ohio State University.

Cell lines and plasmids

Cell lines used in this study including 293T cell line (CRL-3216), B16-OVA cell line (murine melanoma, SCC-420) from Millipore Sigma, MC38 cell line (CVCL-B288), LLC cell line and HT29 cell line from the American Type Culture Collection. 293T, MC38, B16-OVA, LLC and HT29 cells were cultured in Dulbecco's Modified Eagle Medium (Gibco) supplemented with 10% fetal bovine serum (Millipore Sigma), 1% glutamine (Gibco), 1% sodium pyruvate, 1% non-essential amino acids (Gibco), 100 IU/ml penicillin and 100 mg/ml streptomycin (Gibco). The pWPXLd-OGT-GFP fusion vector was described in our previous articles,[2] pET24a-ncOGT-FL (190821, Addgene), other plasmids were cloned into pcDNA3.1 backbone with c-myc or HA tag.

Quantitative Real-Time PCR

Total RNA was extracted from *in vitro* cultured cells and tissues using Trizol reagent (Invitrogen). cDNA synthesis was performed with Moloney murine leukemia virus reverse transcriptase

(Invitrogen) at 38°C for 60 min. RT-PCR was performed using iTaq Universal SYBR Green Supermix in CFX Connect Real-Time PCR Detection System. The fold difference in mRNA expression between treatment groups was determined by a standard $^{\triangle\triangle}$Ct method. *β-actin* and *GAPDH* were analyzed as an internal control. The primer sequences of individual genes are listed in the Supplemental Table 2.

Co-immunoprecipitation (Co-IP) and western blot

For co-immunoprecipitation, cells were lysed in RIPA buffer supplemented with Protease Inhibitor Cocktail. Total protein extracts were incubated with goat anti-GFP Trap agarose (gta-20, Chromotek) or anti-c-Myc Agarose (20168, Thermo Fisher Scientific) overnight at 4°C under gentle agitation. Samples were washed 4 times with cold RIPA buffer. To elute proteins from the beads, samples were incubated with 50 µl of SDS sample buffer at 95°C for 10 min. Protein content in the supernatant was analyzed by western blot. For western blot, electrophoresis of proteins was performed by using the NuPAGE system (Invitrogen) according to the manufacturer's protocol. Briefly, cultured cells were collected and lysed with RIPA buffer. Proteins were separated on a NuPAGE gel and were transferred onto nitrocellulose membranes (Bio-Rad). Appropriate primary antibodies and HRP-conjugated secondary antibodies were used and proteins were detected using the Enhanced Chemiluminescent (ECL) reagent (Thermo Scientific). The images were acquired with ChemiDoc MP System (Bio-Rad). Primary antibodies for western blot included anti-OGT (5368, Cell Signaling Technology), anti-*O*-GlcNAc (ab2739, Abcam), anti-MAVS (sc-365334, Santa Cruz Biotechnology), anti-phospho-TBK1/NAK (Ser172) (5483, Cell Signaling Technology), anti-TBK1 (3504, Cell Signaling Technology), anti-phospho-IRF3 (Ser396) (4947, Cell Signaling Technology), anti-IRF3 (4962, Cell Signaling Technology, anti-anti-phospho-STAT1 (Ser727) (8826S, Cell Signaling Technology), anti-STAT1 (9172, Cell Signaling

Technology), anti-STING (D2P2F) (13647, Cell Signaling Technology), anti-cGAS for mouse (31659S, Cell Signaling Technology), anti-cGAS for human (15102S, Cell Signaling Technology), anti-Phospho-Histone H2AX (Ser139) (MA1-2022, Thermo Fisher Scientific), anti-H2AX (2595S, Cell Signaling Technology), anti-HCFC1 (50708S, Cell Signaling Technology), anti-GFP (sc-9996, Santa Cruz Biotechnology), anti-Actin (sc-1615, Santa Cruz Biotechnology), anti-Myc-peroxidase (11814150001, Millipore Sigma) and anti-HA-HRP (26183, Thermo Fisher Scientific).

***In vitro* pull-down assay**

Recombinant OGT-his purified from *E. coli* system. The recombinant HA-HCF-1^{C600} were expressed in 293T cells and total protein extracts were incubated with Pierce™ Anti-HA Magnetic Beads (88836, Thermo Fisher Scientific) overnight at 4°C under gentle agitation, then competitively with HA Synthetic Peptide (PP100028, Sino Biological) to purify HA-HCF-1^{C600} recombinant protein. Proteins were then mixed with the Ni^{2+} beads for 2 h with rotation at 4°C, The beads were then washed with washed 4 times with cold RIPA buffer, and protein samples were analyzed by western blot and commassie blue staining.

ELISA

Cytokines generated by in vitro cultured tissues from mice were quantified using the ELISA Set for mouse IL-2, IL-6, IL-10, IL-12a, IL-17, IFN-α, IFN-β, IFN-γ, CXCL10 and TNF-α (BD Biosciences) according to the manufacturer's protocol.

Lentivirus-medicated gene knockout in mice and human cell lines

pLenti-CRISPR-V2 vector was used for CRISPR/Cas9-mediated gene knockout in MC38, B16-OVA, LLC and HT29 cell lines, all primers used for sgRNA are listed in the Supplemental Table 3. Briefly, lentivirus vector expressing gRNA was transfected together with package vectors into 293T package cells. 48 h and 72 h after transfection, virus supernatants were harvested and filtrated

with 0.2μm filter. Target cells were infected twice and 2 μg/mL puromycin was added at 3-5 days for selection. After that, the positive cells were diluted into 96-well plates at one cell per well. Isolated single clones were verified by western blot.

Quantification of Cytosolic DNA

For PicoGreen staining, cells were washed twice with cold PBS and fixed with cold methanol at -20°C for 10 minutes. After being washed three times with PBS, cells were blocked with 1% BSA in PBS for 1 h and stained with Pico488 dsDNA quantification reagent for 1 h. After being washed three times with PBS, the dish was mounted on white microscope slides using the Prolong™ Gold Antifade Mountant regent with DAPI and imaged on confocal microscope.

For anti-dsDNA staining, cells were washed with 1 × PBS. Fix the cells with fresh 4% of para-formaldehyde (sc-281692, Santa Cruz Biotechnology) for 10 min at room temperature, then discard the 4% PFA in an appropriate container, wash the cells with 1 × PBS, incubate the cells with the permeabilization buffer for 7 min at room temperature. After three additional washes with 1 × PBS, block nonspecific binding sites by incubating the cells with the blocking buffer for 30 min at room temperature. Remove the blocking buffer (Do not wash). Anti-dsDNA antibody (sc-58749, Santa Cruz Biotechnology) at 1:100 in 1% BSA-PBST.

Incubate samples with diluted anti-dsDNA antibody in humidified chamber overnight at 4 °C. Wash 3 times by 1 × PBS. Dilute the secondary antibody (goat anti-mouse IgG H&L Alexa Fluor® 488 preabsorbed, ab150117, Abcam) at 1:200 in 1% BSA-PBST. Incubate samples with the diluted secondary antibody for 1 h at room temperature. Wash 3 times by 1 × PBS (for 5 min at room temperature). Drop mounting media containing DAPI (Vector laboratories, Vectashield® Hardset™ Anti-fade mounting medium with DAPI, H-1500) on a slide, and put carefully the cover slip. Let it sit for 1–3 h at room temperature. Keep the slide overnight at 4 °C in slide box. Observe

and acquire pictures with a fluorescence microscope using the RFP and DAPI channels the next day to ensure that the mounting medium is completely dry.

Immunohistochemistry (IHC) and immunofluorescence staining

For immunostaining of tissue sections, 5 μm paraffin-embedded sections were cut from paraffin blocks of biopsies. Tissue slides were placed in oven at 60°C for half 1 h and then deparaffinized in xylene 3 times for 5 min each followed by dipping in graded alcohols (100%, 95%, 80% and 70%) 3 times for 2 min each. Slides were washed with distilled water (dH_2O) 3 times for 5 min each and immersed in 3% hydrogen peroxide for 10 min followed by washing with dH_2O. Slides were transferred into pre-heated 0.01M Citrate buffer (pH 6.0) in a steamer for 30 min, and then washed with dH_2O and PBS after cooling. Slides were blocked with 3% BSA/PBS at room temperature for 1 h and then incubated with primary antibody overnight at 4°C, followed by incubating with secondary antibody including Biotinylated Anti-rabbit IgG and Biotinylated Anti-mouse IgG at room temperature for 1h. After incubation with avidin-biotin complex followed by washing 3 × 5 min with PBS, slides were washed with tap water, counterstained with hematoxylin and dipped briefly in graded alcohols (70%, 80%, 95% and 100%) in xylene 2 times for 5 min each. Finally, slides were mounted and imaged by confocal microscopy. For the histological scoring, image J software was used and scored in a blinded fashion using a previously published paper [56].

For the immunofluorescence staining on cells, cells were cultured on the dish. After treatment, cells were washed with PBS, and then fixed with 4% paraformaldehyde (PFA) for 10min, and permeabilized by 0.1% triton X-100. Non-specific binding was blocked through incubation with 5% BSA for 1 h. Cells were stained with anti-γH2AX (05-636-I, Millipore Sigma) overnight at 4°C, and then incubated with fluorochrome-conjugated 2 nd antibodies for 1 h at room

539 temperature. Nucleus was visualized by mounting with DAPI-containing. Finally, cells were
540 imaged by confocal microscopy.

541 For the histological scoring, slides were then examined and scored in a blinded fashion
542 using a previously published grading system [57]. Briefly, histology was scored as follows:–
543 Epithelium (E): 0, normal morphology; 1, loss of goblet cells; 2, loss of goblet cells in large areas;
544 3, loss of crypts; and 4, loss of crypts in large areas. –Infiltration (I): 0, no infiltration; 1, infiltration
545 around crypt bases; 2, infiltration reaching the muscularis mucosa; 3, extensive infiltration
546 reaching the muscularis mucosa and thickening of the mucosa with abundant edema; and 4,
547 infiltration of the submucosa. The total histological score was the sum of the epithelium and
548 infiltration scores (total score = E + I), and thus ranged from 0 to 8.

549 **Comet SCGE assays**

550 Cells were trypsinized to a single cell suspension. Dilute approximat 1:1 in PBS, and immediate
551 place 1 ml of cell suspension in a 1.5 ml tube on mice. Count cells and ensure a density between
552 10^6/ml suspension, add 5 µl cell suspension and 50 µl melted LMAgarose. Mix well and drop it on
553 the slide at 37°C. Place the slides immediately at 4°C for 30 min. Drop slides immersed in cold
554 lysis solution at 4°C for 30 min. After cell lysis, electrophoresis was then carried out in the TBE
555 for 30 min at 35 V voltage. Lastly, DNA was stained with EtBr (20 mg/ml) dye for 10 min. Slides
556 were completely air-dried before taking images. Images were taken by the confocal microscopy
557 and analyzed by using CometScore 2.0.

558 ***In vitro* Cross-Priming of T Cells by BMDCs**

559 BMDCs were prepared by flushing bone marrow from mouse hindlimbs and plating 1×10^6 cells/ml
560 in RPMI 1640 media with 10% FBS and 20 ng/ml mGM-CSF. Fresh medium with mGM-CSF
561 was added into the wells on day 4. On day 6, immature BMDCs were harvested and loaded with

562 1 μg/ml $OVA^{257-264}$ (GenScript), B16-OVA-$Ogt^{+/+}$ and B16-OVA-$Ogt^{-/-}$ cells supernatant at 37°C
563 for 6 h. BMDCs were then washed three times with PBS to remove excessive peptide followed by
564 resuspension in RPMI 160 medium with 10% FBS. OT-I $CD8^+$ T cells were harvested from spleens
565 of wildtype OT-1 mice by $CD8^+$ T Cell Enrichment Kit (Miltenyi), labeled with CFSE with 5 μM
566 CFSE (carboxyfluorescein succinimidyl ester, Life Technologies) in PBS containing 0.1% BSA
567 (Millipore Sigma) for 8 min at 37°C. CFSE-labeled OT-I $CD8^+$ T cells were co-cultured with
568 $OVA^{257-254}$ peptide, B16-OVA-$Ogt^{+/+}$ and B16-OVA-$Ogt^{-/-}$ cells supernatant pulsed BMDCs at a
569 5:1 ratio in 96-well plates. Analysis of the in vitro expansion was performed 48 h after co-culture
570 by enumerating the number of CFSE-diluted $CD8^+$ T cells.

571 **Mass spectrometry assay of OGT interactome**

572 High resolution/accurate mass-based quantitative proteomics strategy was employed to identify
573 protein-protein interactions. Briefly, immunoprecipitated (GFP) OGT complex from $Ogt^{-/-}$+GFP
574 and $Ogt^{-/-}$+OGT-GFP in HT29 cells were boiled with SDS buffer followed by Suspension
575 Trapping based on-filter digestion. The digests were desalted using C18 StageTips, dried in a
576 SpeedVac and then resuspended in 20 μl LC buffer A (0.1% formic acid in water) for LC-MS/MS
577 analysis. The analysis was performed using an Orbitrap Eclipse MS (Thermo Fisher Scientific)
578 coupled with an Ultimate 3000 nanoLC system and a nanospray Flex ion source (Thermo Fisher
579 Scientific). Peptides were first loaded onto a trap column (PepMap C18; 2 cm×100 μm I.D.) and
580 then separated by an analytical column (PepMap C18, 3.0 μm; 20 cm×75mm I.D.) using a binary
581 buffer system (buffer A, 0.1% formic acid in water; buffer B, 0.1% formic acid in acetonitrile)
582 with a 165-min gradient (1% to 25% buffer B over 115 min; 25% to 80% buffer B over 10 min;
583 back to 2% B in 5 min for equilibration after staying on 80% B for 15 min). MS data were acquired
584 in a data-dependent top-12 method with a maximum injection time of 20 ms, a scan range of 350

to 1,800 Da, and an automatic gain control target of 1e6. MS/MS was performed via higher energy collisional dissociation fragmentation with a target value of $5e^5$ and maximum injection time of 100 ms. Full MS and MS/MS scans were acquired by Orbitrap at resolutions of 60,000 and 17,500, respectively. Dynamic exclusion was set to 20 s. Protein identification and quantitation were performed using the MaxQuant-Andromeda software suite (version 1.6.3.4) with most of the default parameters. Other parameters include: trypsin as an enzyme with maximally two missed cleavage sites; protein N-terminal acetylation and methionine oxidation as variable modifications; cysteine carbamidomethylation as a fixed modification; peptide length must be at least 7 amino acids. False discovery rate was set at 1% for both proteins and peptides.

Colitis-associated carcinogenesis (CAC) animal model

The induction of AOM+DSS tumorigenesis model, mice received a single intraperitoneal injection (10 mg/kg body weight) of AOM followed by three cycles of 2.5% DSS exposure for 5 days. Mice were sacrificed and tumor assessments were made 8 weeks after AOM injection. Body weight and tumor number were measured for each animal at the completion of each study. Finally, the colon tissues were collected for further study.

Tumor cell inoculation

For tumor growth, 5×10^5 MC38, LLC and B16-OVA cells were inoculated subcutaneously in the right flank at C57BL/6 mice or *Rag2*$^{-/-}$ mice. For $CD8^+$ and $CD4^+$ T cell depletion, mice were treated with 200 μg of control IgG (clone LTF-2, Bio X cell) or anti-CD8α depleting antibody (clone 2.43, Bio X cell) at day 0, 7 and 14 post tumor cell inoculation. For PD-L1 blockade, mice were intraperitoneally injected with 250 μg of control IgG or anti-PD-L1 antibody (clone 10F.9G2, Bio X Cell) at day 7, 10 and 13 post tumor cell inoculation. For OSMI-1 treatment experiment, OSMI-1 (10 mg/kg) (Aobious, AOB5700) was administered intraperitoneally every two days from

3 to 19 days after post tumor cell inoculation, Digital caliper was used to measure tumor volume at least three times a week and tumor volume were calculated using the formula mm^3 = (Length×width×width/2). Mice were sacrificed at 18 days for flow cytometry and sacrificed when tumors reached a size of 2000 mm^3 for survival curve.

Flow cytometry for TME

Mice tumors were dissected and weighed, then minced into small fragments and digested with 1 mg/mL collagenase IV and 50 U/mL DNase I for 30 min at 37°C. The cell suspensions were mechanically disaggregated and filtered with 100 μm cell strainers. Centrifuge and lysed with the ammonium-chloride-potassium (ACK) lysis buffer for 5 min, then added PBS and passed through 100 μm cell strainers. Single cell suspensions were treated with purified anti-CD16/32 (Fc receptor block, clone 93; BioLegend), and then stained with fluorochrome-conjugated monoclonal antibodies, including anti-CD11b-FITC (M1/70), anti-F4/80-APC (BM8), anti-CD11c-PE-Cy5 (N418), anti-Ly6C-PE (HK1.4), anti-CD4-PE (GK1.5), anti-CD8-APC (53-6.7), anti-CD25-PE-Cy5 (PC61) from BioLegend. For intracellular cytokine staining of tumor-infiltrating lymphocytes (TILs), cells were stimulated *in vitro* with phorbol-12-myristate 13-acetate (PMA) (50 ng/ml, Millipore Sigma) and ionomycin (500 ng/ml, Millipore Sigma) in the presence of GolgiPlug and GolgiStop (BD Biosciences) for 4 h, and then surface stained as aforementioned. Cells were then fixed and permeabilized using BD Cytofix/Cytoperm (BD Biosciences) and stained with anti-IFN-γ (XMG1.2) and anti-TNF-α (MP6-XT22) from BioLegend. For intranuclear Foxp3 staining, single-cell suspensions were stained with antibodies against cell-surface antigens as aforementioned, fixed and permeabilized using Foxp3 Fix/Perm Buffer Kit (BioLegend) followed by staining with Foxp3 (clone MF-14; BioLegend).

Statistics analysis

631 Data were analyzed on GraphPad Prism 8 (GraphPad Software) and R software v4.2.2. The
632 statistical tests, replicate experiments and *P* values are all indicated in the figures and/or legends.
633 *P* values were calculated using two-tailed student's *t* test, one-way ANOVA or two-way ANOVA
634 with Tukey's multiple comparisons test, pearson correlation test, log-rank (Mantel-Cox) test for
635 Kaplan-Meier survival analysis, two-way ANOVA with Sidak's multiple comparisons test or
636 Tukey's multiple comparisons test, Hypergeometric test and adjusted with Benjamini-Hochberg
637 method correction and two-sided Wilcoxon's rank-sum test and adjusted with Bonferroni's
638 correction. Differences between groups are shown as the mean ± SD.
639

References

1. Liu, Y.Y., Liu, H.Y., Yu, T.J., Lu, Q., Zhang, F.L., Liu, G.Y., Shao, Z.M., and Li, D.Q. (2022) **O-GlcNAcylation of MORC2 at threonine 556 by OGT couples TGF-beta signaling to breast cancer progression** *Cell Death and Differentiation*. **29**, 861-873
2. Li, T., Li, X., Attri, K.S., Liu, C., Li, L., Herring, L.E., Asara, J.M., Lei, Y.L., Singh, P.K., Gao, C., and Wen, H. (2018) **O-GlcNAc Transferase Links Glucose Metabolism to MAVS-Mediated Antiviral Innate Immunity** *Cell Host Microbe*. **24**, 791-803 e796
3. Li, X., Gong, W., Wang, H., Li, T., Attri, K.S., Lewis, R.E., Kalil, A.C., Bhinderwala, F., Powers, R., Yin, G., Herring, L.E., Asara, J.M., Lei, Y.L., Yang, X., Rodriguez, D.A., Yang, M., Green, D.R., Singh, P.K., and Wen, H. (2019) **O-GlcNAc Transferase Suppresses Inflammation and Necroptosis by Targeting Receptor-Interacting Serine/Threonine-Protein Kinase 3** *Immunity*. **50**, 576-590 e576
4. Zhu, Y., and Hart, G.W. (2023) **Dual-specificity RNA aptamers enable manipulation of target-specific O-GlcNAcylation and unveil functions of O-GlcNAc on beta-catenin** *Cell*. **186**, 428-445 e427
5. Mi, W., Gu, Y., Han, C., Liu, H., Fan, Q., Zhang, X., Cong, Q., and Yu, W. (2011) **O-GlcNAcylation is a novel regulator of lung and colon cancer malignancy** *Biochim Biophys Acta*. **1812**, 514-519
6. Phueaouan, T., Chaiyawat, P., Netsirisawan, P., Chokchaichamnankit, D., Punyarit, P., Srisomsap, C., Svasti, J., and Champattanachai, V. (2013) **Aberrant O-GlcNAc-modified proteins expressed in primary colorectal cancer** *Oncol Rep*. **30**, 2929-2936
7. Olivier-Van Stichelen, S., Dehennaut, V., Buzy, A., Zachayus, J.L., Guinez, C., Mir, A.M., El Yazidi-Belkoura, I., Copin, M.C., Boureme, D., Loyaux, D., Ferrara, P., and Lefebvre, T. (2014) **O-GlcNAcylation stabilizes beta-catenin through direct competition with phosphorylation at threonine 41** *FASEB journal : official publication of the Federation of American Societies for Experimental Biology*. **28**, 3325-3338
8. Fardini, Y., Dehennaut, V., Lefebvre, T., and Issad, T. (2013) **O-GlcNAcylation: A New Cancer Hallmark** *Front Endocrinol (Lausanne)*. **4**, 99
9. Chaiyawat, P., Netsirisawan, P., Svasti, J., and Champattanachai, V. (2014) **Aberrant O-GlcNAcylated Proteins: New Perspectives in Breast and Colorectal Cancer** *Front Endocrinol (Lausanne)*. **5**, 193
10. Ozcan, S., Andrali, S.S., and Cantrell, J.E.L. (2010) **Modulation of transcription factor function by O-GlcNAc modification** *Bba-Gene Regul Mech*. **1799**, 353-364
11. Olivier-Van Stichelen, S., Guinez, C., Mir, A.M., Perez-Cervera, Y., Liu, C., Michalski, J.C., and Lefebvre, T. (2012) **The hexosamine biosynthetic pathway and O-GlcNAcylation drive the expression of beta-catenin and cell proliferation** *Am J Physiol Endocrinol Metab*. **302**, E417-424
12. Yehezkel, G., Cohen, L., Kliger, A., Manor, E., and Khalaila, I. (2012) **O-linked beta-N-acetylglucosaminylation (O-GlcNAcylation) in primary and metastatic colorectal cancer clones and effect of N-acetyl-beta-D-glucosaminidase silencing on cell phenotype and transcriptome** *J Biol Chem*. **287**, 28755-28769
13. Wu, J., Bowe, D.B., Sadlonova, A., Whisenhunt, T.R., Hu, Y., Rustgi, A.K., Nie, Y., Paterson, A.J., and Yang, X. (2014) **O-GlcNAc transferase is critical for transducin-like enhancer of split (TLE)-mediated repression of canonical Wnt signaling** *J Biol Chem*. **289**, 12168-12176

14. Li, S., Kong, L., Meng, Y., Cheng, C., Lemacon, D.S., Yang, Z., Tan, K., Cheruiyot, A., Lu, Z., and You, Z. (2023) **Cytosolic DNA sensing by cGAS/STING promotes TRPV2-mediated Ca(2+) release to protect stressed replication forks** *Mol Cell*. **83**, 556-573 e557
15. Ghosh, M., Saha, S., Bettke, J., Nagar, R., Parrales, A., Iwakuma, T., van der Velden, A.W.M., and Martinez, L.A. (2021) **Mutant p53 suppresses innate immune signaling to promote tumorigenesis** *Cancer Cell*. **39**, 494-508 e495
16. Fang, R., Jiang, Q., Jia, X., and Jiang, Z. (2023) **ARMH3-mediated recruitment of PI4KB directs Golgi-to-endosome trafficking and activation of the antiviral effector STING** *Immunity*. **56**, 500-515 e506
17. Kwon, J., and Bakhoum, S.F. (2020) **The Cytosolic DNA-Sensing cGAS-STING Pathway in Cancer** *Cancer Discov*. **10**, 26-39
18. Gu, Y., Mi, W., Ge, Y., Liu, H., Fan, Q., Han, C., Yang, J., Han, F., Lu, X., and Yu, W. (2010) **GlcNAcylation plays an essential role in breast cancer metastasis** *Cancer Res*. **70**, 6344-6351
19. Itkonen, H.M., Minner, S., Guldvik, I.J., Sandmann, M.J., Tsourlakis, M.C., Berge, V., Svindland, A., Schlomm, T., and Mills, I.G. (2013) **O-GlcNAc transferase integrates metabolic pathways to regulate the stability of c-MYC in human prostate cancer cells** *Cancer Res*. **73**, 5277-5287
20. Jiang, M., Xu, B., Li, X., Shang, Y., Chu, Y., Wang, W., Chen, D., Wu, N., Hu, S., Zhang, S., Li, M., Wu, K., Yang, X., Liang, J., Nie, Y., and Fan, D. (2019) **O-GlcNAcylation promotes colorectal cancer metastasis via the miR-101-O-GlcNAc/EZH2 regulatory feedback circuit** *Oncogene*. **38**, 301-316
21. Yi, W., Clark, P.M., Mason, D.E., Keenan, M.C., Hill, C., Goddard, W.A., 3rd, Peters, E.C., Driggers, E.M., and Hsieh-Wilson, L.C. (2012) **Phosphofructokinase 1 glycosylation regulates cell growth and metabolism** *Science*. **337**, 975-980
22. Yang, X.Y., and Qian, K.V. (2017) **Protein O-GlcNAcylation: emerging mechanisms and functions** *Nat Rev Mol Cell Bio*. **18**, 452-465
23) McNab, F., Mayer-Barber, K., Sher, A., Wack, A., and O'Garra, A. (2015) **Type I interferons in infectious disease** *Nat Rev Immunol*. **15**, 87-103
24. Liu, S., Cai, X., Wu, J., Cong, Q., Chen, X., Li, T., Du, F., Ren, J., Wu, Y.T., Grishin, N.V., and Chen, Z.J. (2015) **Phosphorylation of innate immune adaptor proteins MAVS, STING, and TRIF induces IRF3 activation** *Science*. **347**, aaa2630
25. Gui, X., Yang, H., Li, T., Tan, X., Shi, P., Li, M., Du, F., and Chen, Z.J. (2019) **Autophagy induction via STING trafficking is a primordial function of the cGAS pathway** *Nature*. **567**, 262-266
26. Gonugunta, V.K., Sakai, T., Pokatayev, V., Yang, K., Wu, J., Dobbs, N., and Yan, N. (2017) **Trafficking-Mediated STING Degradation Requires Sorting to Acidified Endolysosomes and Can Be Targeted to Enhance Anti-tumor Response** *Cell Rep*. **21**, 3234-3242
27. Zhu, Y., An, X., Zhang, X., Qiao, Y., Zheng, T., and Li, X. (2019) **STING: a master regulator in the cancer-immunity cycle** *Mol Cancer*. **18**, 152
28. Joffre, O.P., Segura, E., Savina, A., and Amigorena, S. (2012) **Cross-presentation by dendritic cells** *Nat Rev Immunol*. **12**, 557-569
29. Zitvogel, L., Galluzzi, L., Kepp, O., Smyth, M.J., and Kroemer, G. (2015) **Type I interferons in anticancer immunity** *Nat Rev Immunol*. **15**, 405-414

30. Woo, S.R., Fuertes, M.B., Corrales, L., Spranger, S., Furdyna, M.J., Leung, M.Y., Duggan, R., Wang, Y., Barber, G.N., Fitzgerald, K.A., Alegre, M.L., and Gajewski, T.F. (2014) **STING-dependent cytosolic DNA sensing mediates innate immune recognition of immunogenic tumors** *Immunity*. **41**, 830-842
31. Xu, M.M., Pu, Y., Han, D., Shi, Y., Cao, X., Liang, H., Chen, X., Li, X.D., Deng, L., Chen, Z.J., Weichselbaum, R.R., and Fu, Y.X. (2017) **Dendritic Cells but Not Macrophages Sense Tumor Mitochondrial DNA for Cross-priming through Signal Regulatory Protein alpha Signaling** *Immunity*. **47**, 363-373 e365
32. Li, T., and Chen, Z.J. (2018) **The cGAS-cGAMP-STING pathway connects DNA damage to inflammation, senescence, and cancer** *J Exp Med*. **215**, 1287-1299
33. Shen, Y.J., Le Bert, N., Chitre, A.A., Koo, C.X., Nga, X.H., Ho, S.S., Khatoo, M., Tan, N.Y., Ishii, K.J., and Gasser, S. (2015) **Genome-derived cytosolic DNA mediates type I interferon-dependent rejection of B cell lymphoma cells** *Cell Rep*. **11**, 460-473
34. Lu, C., Guan, J., Lu, S., Jin, Q., Rousseau, B., Lu, T., Stephens, D., Zhang, H., Zhu, J., Yang, M., Ren, Z., Liang, Y., Liu, Z., Han, C., Liu, L., Cao, X., Zhang, A., Qiao, J., Batten, K., Chen, M., Castrillon, D.H., Wang, T., Li, B., Diaz, L.A., Jr., Li, G.M., and Fu, Y.X. (2021) **DNA Sensing in Mismatch Repair-Deficient Tumor Cells Is Essential for Anti-tumor Immunity** *Cancer Cell*. **39**, 96-108 e106
35. Chowdhury, D., Keogh, M.C., Ishii, H., Peterson, C.L., Buratowski, S., and Lieberman, J. (2005) **gamma-H2AX dephosphorylation by protein phosphatase 2A facilitates DNA double-strand break repair** *Molecular Cell*. **20**, 801-809
36. Capotosti, F., Guernier, S., Lammers, F., Waridel, P., Cai, Y., Jin, J., Conaway, J.W., Conaway, R.C., and Herr, W. (2011) **O-GlcNAc transferase catalyzes site-specific proteolysis of HCF-1** *Cell*. **144**, 376-388
37. Yost, K.E., Satpathy, A.T., Wells, D.K., Qi, Y., Wang, C., Kageyama, R., McNamara, K.L., Granja, J.M., Sarin, K.Y., Brown, R.A., Gupta, R.K., Curtis, C., Bucktrout, S.L., Davis, M.M., Chang, A.L.S., and Chang, H.Y. (2019) **Clonal replacement of tumor-specific T cells following PD-1 blockade** *Nat Med*. **25**, 1251-1259
38. Patel, S.A., and Minn, A.J. (2018) **Combination Cancer Therapy with Immune Checkpoint Blockade: Mechanisms and Strategies** *Immunity*. **48**, 417-433
39. Brahmer, J.R., Tykodi, S.S., Chow, L.Q., Hwu, W.J., Topalian, S.L., Hwu, P., Drake, C.G., Camacho, L.H., Kauh, J., Odunsi, K., Pitot, H.C., Hamid, O., Bhatia, S., Martins, R., Eaton, K., Chen, S., Salay, T.M., Alaparthy, S., Grosso, J.F., Korman, A.J., Parker, S.M., Agrawal, S., Goldberg, S.M., Pardoll, D.M., Gupta, A., and Wigginton, J.M. (2012) **Safety and activity of anti-PD-L1 antibody in patients with advanced cancer** *N Engl J Med*. **366**, 2455-2465
40. Topalian, S.L., Drake, C.G., and Pardoll, D.M. (2012) **Targeting the PD-1/B7-H1(PD-L1) pathway to activate anti-tumor immunity** *Curr Opin Immunol*. **24**, 207-212
41. Ortiz-Meoz, R.F., Jiang, J.Y., Lazarus, M.B., Orman, M., Janetzko, J., Fan, C.G., Duveau, D.Y., Tan, Z.W., Thomas, C.J., and Walker, S. (2015) **A Small Molecule That Inhibits OGT Activity in Cells** *Acs Chemical Biology*. **10**, 1392-1397
42. Chen, Q., Sun, L., and Chen, Z.J. (2016) **Regulation and function of the cGAS-STING pathway of cytosolic DNA sensing** *Nat Immunol*. **17**, 1142-1149
43. Clementi, E., Inglin, L., Beebe, E., Gsell, C., Garajova, Z., and Markkanen, E. (2020) **Persistent DNA damage triggers activation of the integrated stress response to promote cell survival under nutrient restriction** *BMC Biol*. **18**, 36

44. Lan, Y.Y., Londono, D., Bouley, R., Rooney, M.S., and Hacohen, N. (2014) **Dnase2a Deficiency Uncovers Lysosomal Clearance of Damaged Nuclear DNA via Autophagy** *Cell Reports*. **9**, 180-192
45. Hartlova, A., Erttmann, S.F., Raffi, F.A.M., Schmalz, A.M., Resch, U., Anugula, S., Lienenklaus, S., Nilsson, L.M., Kroger, A., Nilsson, J.A., Ek, T., Weiss, S., and Gekara, N.O. (2015) **DNA Damage Primes the Type I Interferon System via the Cytosolic DNA Sensor STING to Promote Anti-Microbial Innate Immunity** *Immunity*. **42**, 332-343
46. Yang, H., Wang, H.Z., Ren, J.Y., Chen, Q., and Chen, Z.J.J. (2017) **cGAS is essential for cellular senescence** *P Natl Acad Sci USA*. **114**, E4612-E4620
47. Gluck, S., Guey, B., Gulen, M.F., Wolter, K., Kang, T.W., Schmacke, N.A., Bridgeman, A., Rehwinkel, J., Zender, L., and Ablasser, A. (2017) **Innate immune sensing of cytosolic chromatin fragments through cGAS promotes senescence** *Nature Cell Biology*. **19**, 1061-+
48. Harding, S.M., Benci, J.L., Irianto, J., Discher, D.E., Minn, A.J., and Reenberg, R.A.G. (2017) **Mitotic progression following DNA damage enables pattern recognition within micronuclei** *Nature*. **548**, 466-+
49. Mackenzie, K.J., Carroll, P., Martin, C.A., Murina, O., Fluteau, A., Impson, D.J.S., Olova, N., Sutcliffe, H., Rainger, J.K., Leitch, A., Osborn, R.T., Wheeler, A.P., Nowotny, M., Gilbert, N., Chandra, T., Reijns, M.A.M., and Jackson, A.P. (2017) **cGAS surveillance of micronuclei links genome instability to innate immunity** *Nature*. **548**, 461-+
50. Li, X.D., Wu, J., Gao, D., Wang, H., Sun, L., and Chen, Z.J. (2013) **Pivotal roles of cGAS-cGAMP signaling in antiviral defense and immune adjuvant effects** *Science*. **341**, 1390-1394
51. Deng, L., Liang, H., Xu, M., Yang, X., Burnette, B., Arina, A., Li, X.D., Mauceri, H., Beckett, M., Darga, T., Huang, X., Gajewski, T.F., Chen, Z.J., Fu, Y.X., and Weichselbaum, R.R. (2014) **STING-Dependent Cytosolic DNA Sensing Promotes Radiation-Induced Type I Interferon-Dependent Antitumor Immunity in Immunogenic Tumors** *Immunity*. **41**, 843-852
52. Guan, J., Lu, C., Jin, Q., Lu, H., Chen, X., Tian, L., Zhang, Y., Ortega, J., Zhang, J., Siteni, S., Chen, M., Gu, L., Shay, J.W., Davis, A.J., Chen, Z.J., Fu, Y.X., and Li, G.M. (2021) **MLH1 Deficiency-Triggered DNA Hyperexcision by Exonuclease 1 Activates the cGAS-STING Pathway** *Cancer Cell*. **39**, 109-121 e105
53. Zhang, W., Liu, W., Jia, L., Chen, D., Chang, I., Lake, M., Bentolila, L.A., and Wang, C.Y. (2021) **Targeting KDM4A epigenetically activates tumor-cell-intrinsic immunity by inducing DNA replication stress** *Mol Cell*. **81**, 2148-2165 e2149
54. Jenkins, R.W., Barbie, D.A., and Flaherty, K.T. (2018) **Mechanisms of resistance to immune checkpoint inhibitors** *Br J Cancer*. **118**, 9-16
55. Murciano-Goroff, Y.R., Warner, A.B., and Wolchok, J.D. (2020) **The future of cancer immunotherapy: microenvironment-targeting combinations** *Cell Res*. **30**, 507-519
56. Young, K., and Morrison, H. (2018) **Quantifying Microglia Morphology from Photomicrographs of Immunohistochemistry Prepared Tissue Using ImageJ** *J Vis Exp*.
57. Takagi, T., Naito, Y., Uchiyama, K., Suzuki, T., Hirata, I., Mizushima, K., Tsuboi, H., Hayashi, N., Handa, O., Ishikawa, T., Yagi, N., Kokura, S., Ichikawa, H., and Yoshikawa, T. (2011) **Carbon monoxide liberated from carbon monoxide-releasing molecule**

exerts an anti-inflammatory effect on dextran sulfate sodium-induced colitis in mice *Dig Dis Sci*. **56**, 1663-1671

Figure Legends

Fig. 1 OGT is significantly upregulated in human and mouse tumor samples.

(A-C) Boxplot showing mRNA expression level of *Ogt*, Normal and tumor samples (A), Individual stages (**B**), Nodal metastasis status (**C**). The plot was generated using the UALCAN online server. **D-E**) Boxplot showing protein expression level of OGT, Normal and tumor samples (**A**), Individual stages (**B**). The plot was generated using the UALCAN online server (https://ualcan.path.uab.edu/analysis.html). **F**) IHC analysis of OGT expression in normal colon tissues, primary colon tumor samples (from Human Protein Atlas, https://www.proteinatlas.org/), scale bar: 400μm. **G**) Western blot analysis of OGT and *O*-GlcNAc expression in normal, adjacent and tumor tissues in Apc^{min} spontaneous tumor mice. **H**) HE and IHC staining of OGT in adjacent and tumor tissues in Apc^{min} spontaneous tumor mice, scale bar: left panel 275 μm, right panel 75μm, n=3 respectively. **I**) Schematic of AOM/DSS model of colitis-associated colorectal cancer (CAC). **J**) Western blot analysis of OGT and *O*-GlcNAc expression in normal, adjacent and tumor tissues in CAC model. **K**) HE and IHC staining of OGT in adjacent and tumor tissues in CAC model, scale bar: left panel 275 μm, right panel 75μm, n=4 respectively. human samples (**A-F**), mouse samples (**G-K**). Statistical significance was determined by Pearson test, unpaired Student's t-test, $*p < 0.05$, $**p < 0.01$, $***p < 0.001$, ns, no significant difference. Data represent the mean of ± SD.

Fig. 2 Epithelial OGT deletion inhibits mouse colorectal tumorigenesis.

A) Western blot analysis of OGT expression in intestinal tissues and counting tumor numbers in APC^{min} and $Ogt^{\triangle IEC}$ mice. **B**) Histology analysis of intestinal carcinogenesis by HE staining, scale bar: up panel 275 μm, bottom panel 20 μm, n=3 respectively. **C**) Real-time PCR analysis of

869 cytokines mRNA expression in intestine. **D**) ELISA analysis of cytokines expression in intestine.
870 Statistical significance was determined by unpaired Student's t-test, *$p < 0.05$, **$p < 0.01$, ***p
871 < 0.001, ns, no significant difference. Data represent the mean of ± SD.
872
873 **Fig. 3 OGT deficiency induces cGAS/STING-dependent the type I IFN pathway.**
874 **A-D**) Real-time PCR analysis of cytokines mRNA expression in different *Ogt*$^{-/-}$ cell lines
875 including MC38 (**A**), LLC (**B**), HT29 (**C**), B16-OVA (**D**) cells. **E**) Western blot analysis of the
876 activation of the interferon signaling pathway in different *Ogt*$^{-/-}$ cell lines including MC38, LLC
877 and B16-OVA cells. **F**) Western blot analysis of the activation of the interferon signaling pathway
878 in *Ogt*$^{-/-}$ rescued cell lines including MC38, LLC, HT29 and B16-OVA cells. **G-H**) Real-time
879 PCR and western blot analysis of cytokines mRNA expression and the activation of the interferon
880 signaling pathway in different *Ogt*$^{-/-}$*Mavs*$^{-/-}$ double knockout clones in MC38 cells. **I-K**) Real-
881 time PCR and ELISA analysis of cytokines mRNA expression in *Ogt*$^{-/-}$*cGAS*$^{-/-}$ double knockout
882 clones in MC38 (**I-J**), HT29 (**K**) cells. **L**) Western blot analysis of the activation of the interferon
883 signaling pathway in *Ogt*$^{-/-}$*cGAS*$^{-/-}$ or *Ogt*$^{-/-}$*Sting*$^{-/-}$ double knockout clones in MC38, HT29 and
884 B16-OVA cells. **M-N**) BMDCs pre-treated with B16-OVA-*Ogt*$^{-/-}$ (**L**), B16-OVA-*Ogt*$^{-/-}$*cGAS*$^{-/-}$
885 or B16-OVA-*Ogt*$^{-/-}$*Sting*$^{-/-}$ cells (**M**) supernatant, and co-cultured with OT-1 T cell, then T cell
886 proliferation was evaluated by flow cytometry, OVA$^{257-264}$ as a positive control. Representative
887 fluorescence-activated cell sorting histograms and statistical data are shown. Data are
888 representative of two or three independent experiments. Statistical significance was determined by
889 unpaired Student's t-test, one-way ANOVA, two-way ANOVA, *$p < 0.05$,**$p < 0.01$,***$p <$
890 0.001, ns, no significant difference. Data represent the mean of ± SD.
891

Fig. 4 OGT deficiency causes DNA damage and accumulates cytosolic DNA.

A) The extranuclear dsDNA in different *Ogt*$^{-/-}$ MC38 cells clones were determined by PicoGreen staining assay was quantified by image J. **B**) The extranuclear dsDNA in different *Ogt*$^{-/-}$ MC38 cells clones were determined by anti-dsDNA fluorescence staining assay and was quantified by image J. **C**) Western blot analysis of γH2AX and H2AX expression in different *Ogt*$^{-/-}$ cell lines including MC38, LLC and B16-OVA cells. **D**) Analysis of γH2AX and H2AX expression in different *Ogt*$^{-/-}$ clones by anti-γH2AX staining assay and was quantified by image J. **E**) The DNA damage was determined by comet assay, and extranuclear dsDNA was analyzed by using CometScore in *Ogt*$^{-/-}$ MC38 cells. **F**) Western blot analysis of γH2AX and H2AX expression in *Ogt*$^{-/-}$ rescued cells including MC38, LLC, HT29 and B16-OVA cells. **G**) The DNA damage in rescued MC38 cells were determined by comet assay, and extranuclear dsDNA was analyzed by using CometScore. Data are representative of three or four independent experiments. Statistical significance was determined by unpaired Student's t-test, one-way ANOVA, *$p < 0.05$, **$p < 0.01$, ***$p < 0.001$, ns, no significant difference. Data represent the mean of ± SD.

Fig. 5 The C terminal of HCF-1 rescue DNA damage and the type I IFN pathway in *Ogt*$^{-/-}$ cells.

A) Volcano plot of OGT binding proteins identified by LC–MS/MS from stably expressed exogenous GFP-OGT in OGT knockout HT29 cells. **B**) OGT and HCF1 binding was confirmed by immunoprecipitation assay in OGT rescued HT29 cells. **C**) OGT and HCF1 binding was confirmed by immunoprecipitation assay in 293T cells. **D**) HCF1 cleavage was confirmed by western blot in *Ogt* rescued MC38 cells. **E**) Co-IP analysis of the interaction between OGT and different HCF-1 mutant. **F**) Real-time PCR analysis of cytokines mRNA expression effected by

HCF-1 isoforms in MC38 OGT knockout cells. **G**) Western blot analysis of γH2AX and H2AX expression in exogenous HCF-1^{C600} expressed MC38 *Ogt* knockout cells. **H**) The extranuclear dsDNA were determined by anti-dsDNA fluorescence staining assay and was quantified by image J in exogenous HCF-1^{C600} expressed MC38 OGT knockout cells. Data are representative of three or four independent experiments. Statistical significance was determined by one-way ANOVA, two-way ANOVA, $*p < 0.05$, $**p < 0.01$, $***p < 0.001$, ns, no significant difference. Data represent the mean of ± SD.

Fig. 6 *Ogt* deficiency inhibits tumor progression through enhancing infiltration by $CD8^+$ T cells.

A-B) Tumor volume, weight of $Ogt^{+/+}$ or $Ogt^{-/-}$ MC38 tumors in C57BL/6J mice and mice survival, n=5 respectively. **C-D**) Tumor volume, weight of $Ogt^{+/+}$ or $Ogt^{-/-}$ LLC tumors in C57BL/6J mice and mice survival, n=5 respectively. **E-H**) Flow cytometry analysis of percentage of $CD4^+$ and $CD8^+$ T cells population(**E**) and IFN-γ^+ (**F**), TNF-α^+ (**G**), IFN-γ^+TNF-α^+ double positive (**H**) intratumoral $CD8^+$ T cells population in MC38 tumors, subcutaneous tumor isolated at day 18 post-tumor inoculation, n=5 respectively. **I**) Tumor volume and weight of $Ogt^{+/+}$ or $Ogt^{-/-}$ MC38 in $Rag2^{-/-}$ mice, n=5 respectively. **J-K**) Tumor volume, weight of $Ogt^{+/+}$ or $Ogt^{-/-}$ MC38 tumors injected with either control IgG or anti-CD8α at day 0, 7 and 14 post tumor inoculation in C57BL/6J mice and mice survival, n=5 respectively. **L-M**) Tumor volume, weight of $Ogt^{-/-}$ rescued MC38 tumors in C57BL/6J mice, tumor growth volume and weight (**L**), mice survival (**M**). **N-O**) Tumor volume, weight of $Ogt^{-/-}cGAS^{-/-}$ or $Ogt^{-/-}Sting^{-/-}$ double knockout MC38 tumors in C57BL/6J mice, tumor growth volume and weight (**N**), mice survival (**O**). **P**) Flow cytometry analysis showing percentage of $CD4^+$ and $CD8^+$ T cells population (**N**), $CD8^+$ IFN-γ^+ (**O**), $CD8^+$

TNF-α^+ T cell population (**P**) in *Ogt*$^{-/-}$*cGAS*$^{-/-}$ or *Ogt*$^{-/-}$*Sting*$^{-/-}$ double knockout MC38 tumors in C57BL/6J mice, subcutaneous tumor isolated at day 18 post-tumor inoculation. **Q-R**) Tumor volume, weight of *Ogt*$^{+/+}$ or *Ogt*$^{-/-}$ MC38 tumors injected with either control IgG or anti-PD-L1 at day 7, 10 and 13 post tumor inoculation in C57BL/6J mice and mice survival, n=5 respectively. **S**) Kaplan-Meier survival curves for colorectal cancer patients with low (n=207) or high (n=231) *OGT* transcripts in TCGA dataset. T) Progression-free survival curves for colorectal cancer patients with low (n=58) or high (n=58) *OGT* transcripts in TCGA dataset. **U**) Scatterplot presenting the association between the mRNA expression level of *OGT* and $CD8^+$ T infiltration, Spearman's r = -0.263, p = 9.75E-6, Spearman's rank correlation test. Data are representative of two or three independent experiments. Statistical significance was determined by Spearman's rank correlation test, unpaired Student's t-test, one-way ANOVA, two-way ANOVA, *$p < 0.05$, **$p < 0.01$, ***$p < 0.001$, ns, no significant difference. Data represent the mean of ± SD.

Fig. 7 Combination therapy with OSMI-1 and anti-PD-L1 augmented T cells and antitumor immunity.

A) The extranuclear dsDNA were determined by anti-dsDNA fluorescence staining treated with 50 μM and 100 μM OSMI in MC38 cells respectively and was quantified by image J. **B-C**) Western blot analysis of protein expression in MC38 and LLC cells treated with 50 μM and 100 μM OSMI, respectively. **D**) Analysis of γH2AX and H2AX expression by anti-γH2AX staining treated with 50 μM and 100 μM OSMI in MC38 cells and was quantified by image J. **E-F**) Tumor volume, weight of MC38 tumors injected with either control OSMI-1 or anti-PD-L1 in C57BL/6J mice and mice survival. **G-H**) Tumor volume, weight of LLC tumors injected with either control OSMI-1 or anti-PD-L1 in C57BL/6J mice and mie survival. **I-K**) Flow cytometry analysis showing

961 percentage of $CD4^+$ and $CD8^+$ T cells population (**I**), and $CD8^+$ IFN-γ^+ cells (**J**), $CD8^+$ TNF-α^+
962 cells (**K**) population in MC38 subcutaneous tumor isolated at day 18 post-tumor inoculation. **L-N**)
963 Flow cytometry analysis showing percentage of $CD4^+$ and $CD8^+$ T cells population (L), and $CD8^+$
964 IFN-γ^+ cells (**M**), $CD8^+$ TNF-α^+ cells (**N**) population in LLC subcutaneous tumor isolated at day
965 18 post-tumor inoculation. Data are representative of three or four independent experiments.
966 Statistical significance was determined by unpaired Student's t-test, one-way ANOVA, two-way
967 ANOVA, $*p < 0.05$, $**p < 0.01$, $***p < 0.001$, ns, no significant difference. Data represent the
968 mean of ± SD.

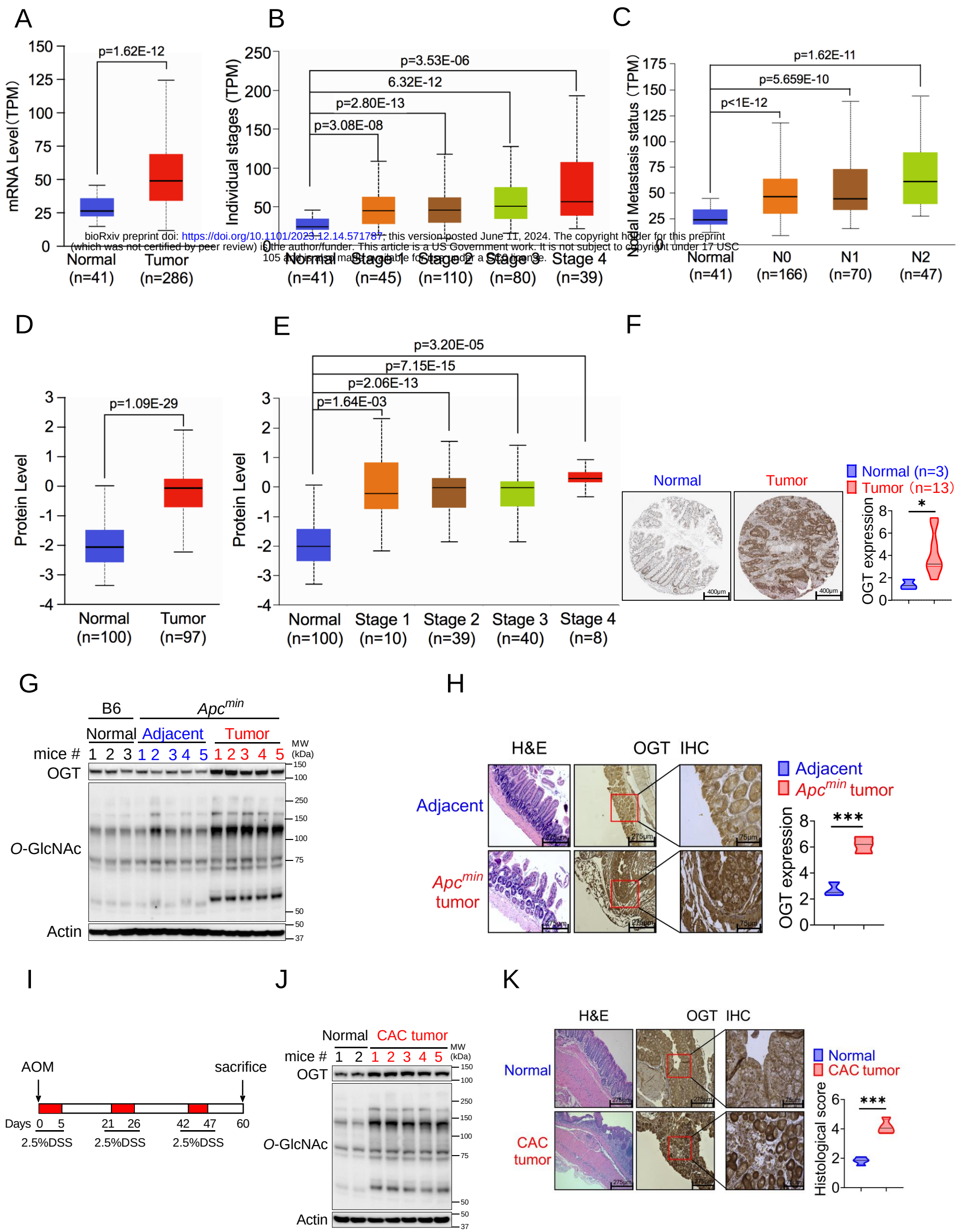

Figure 1

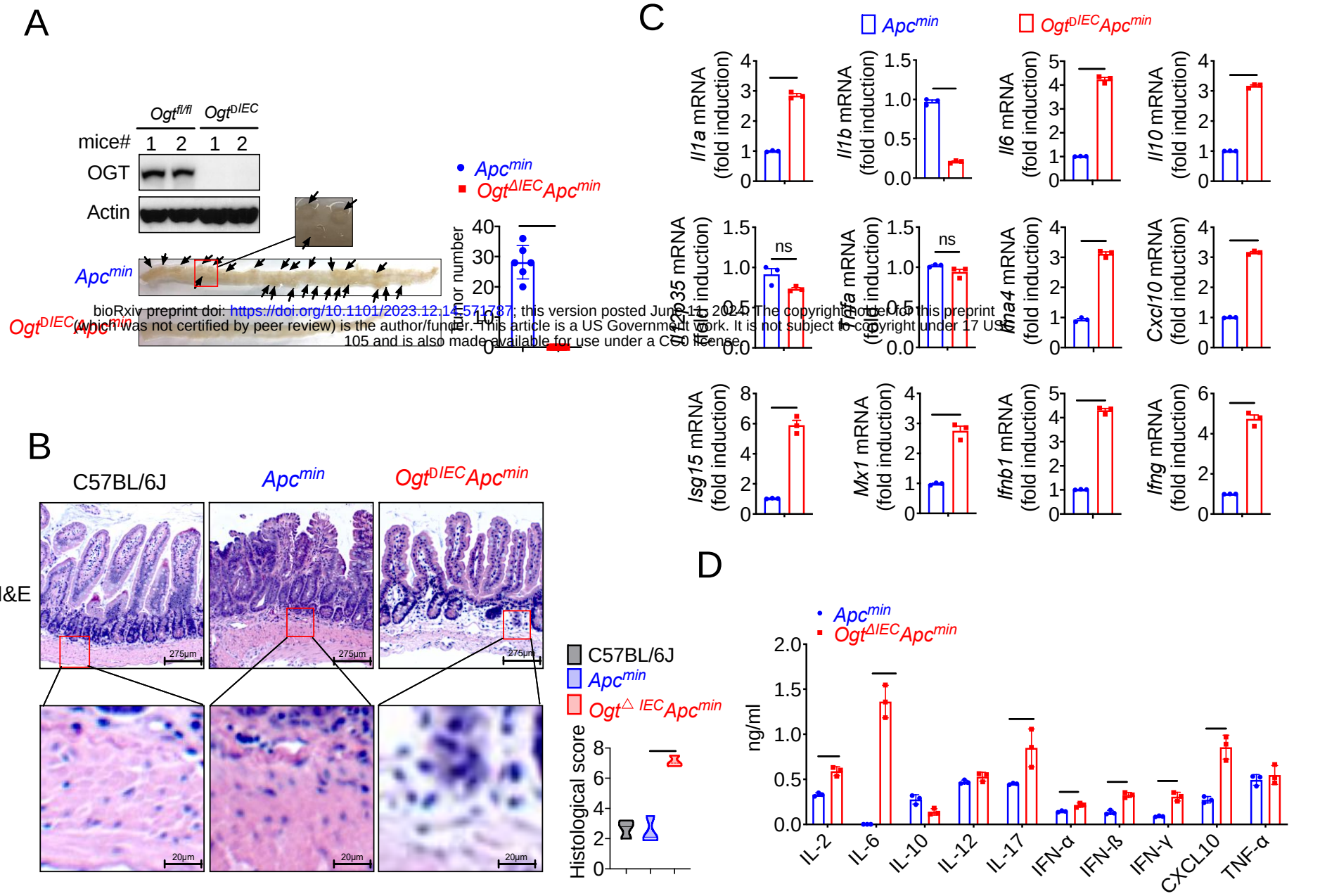

Figure 2

Figure 3

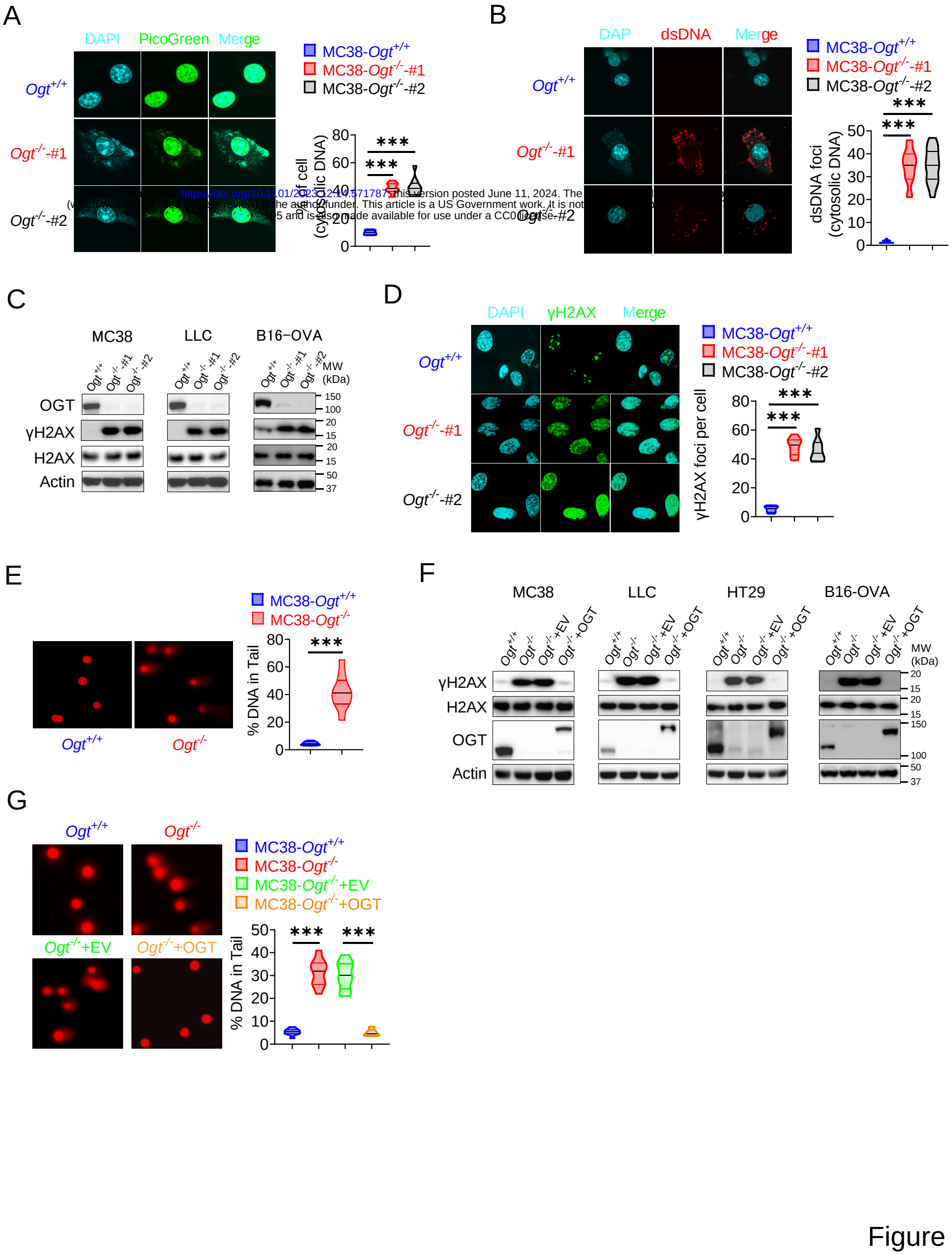

Figure 4

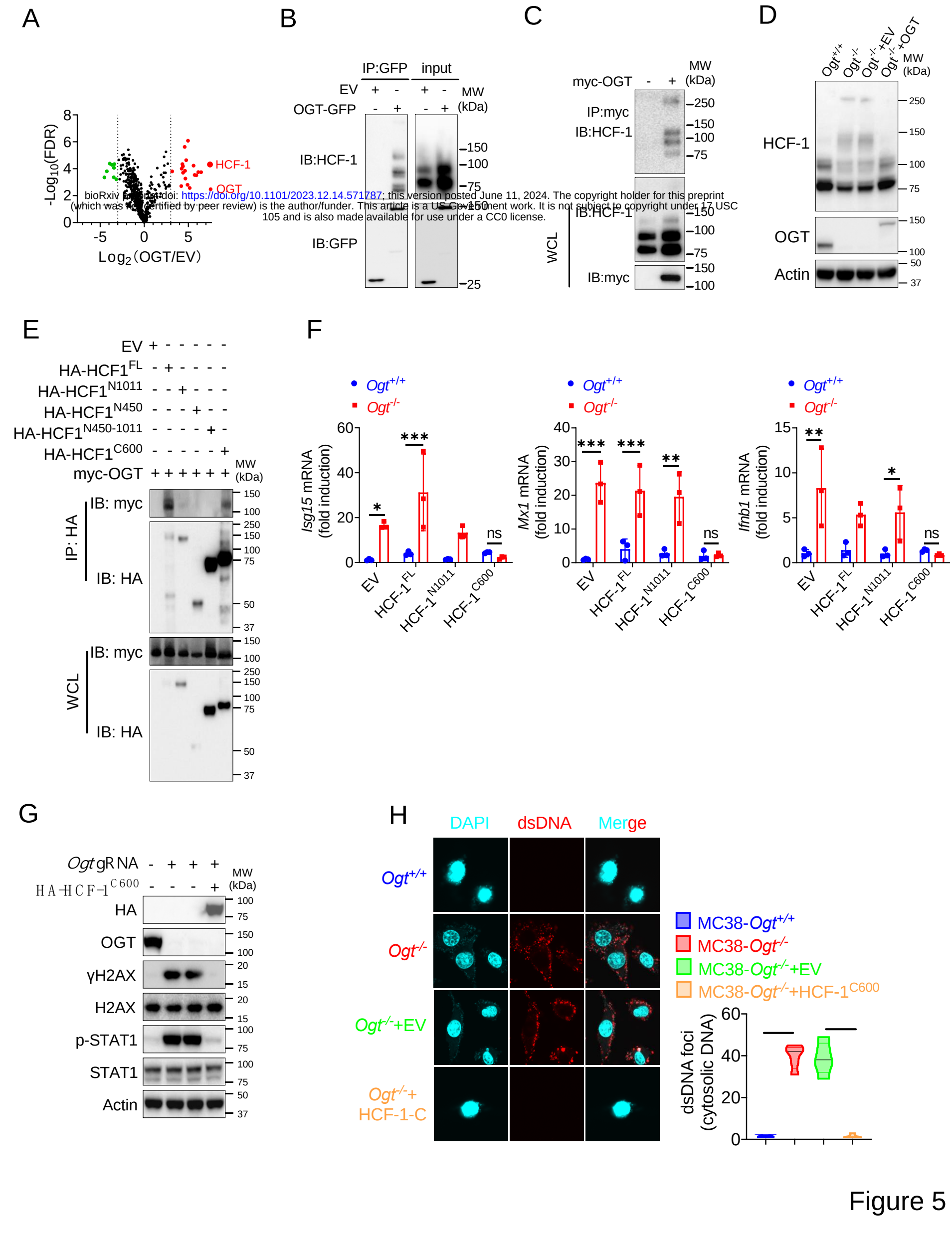

Figure 5

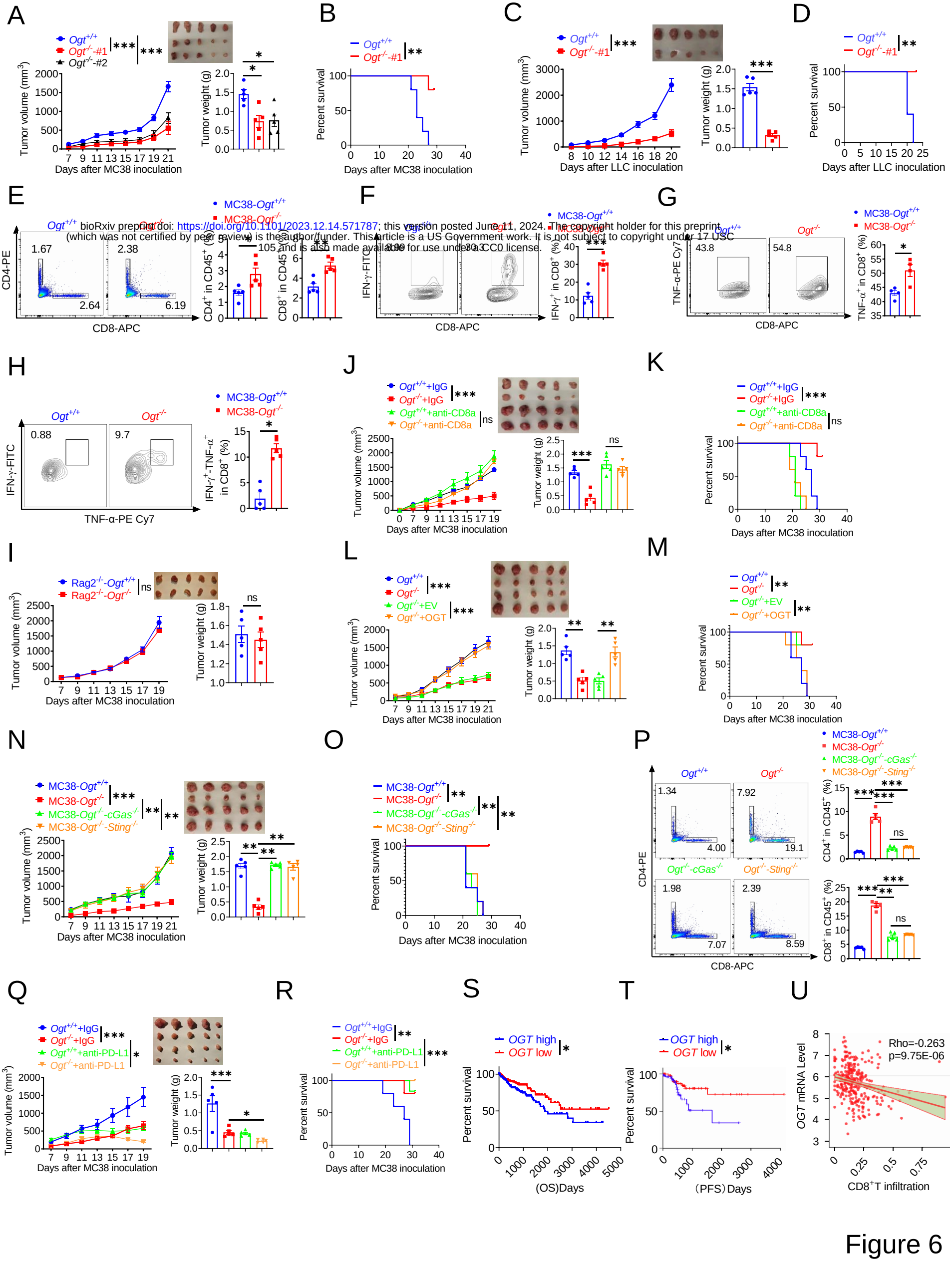

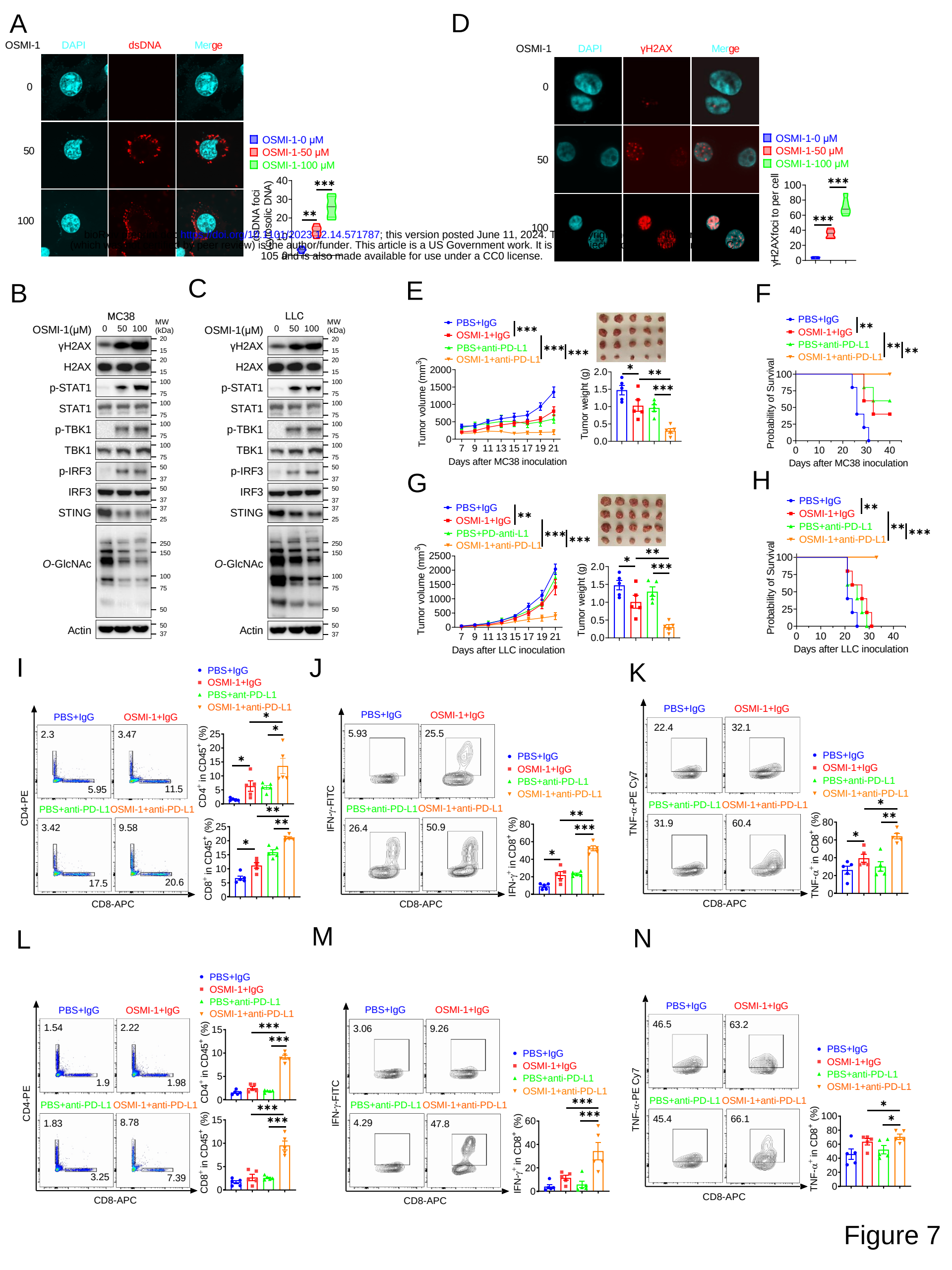

Figure 7

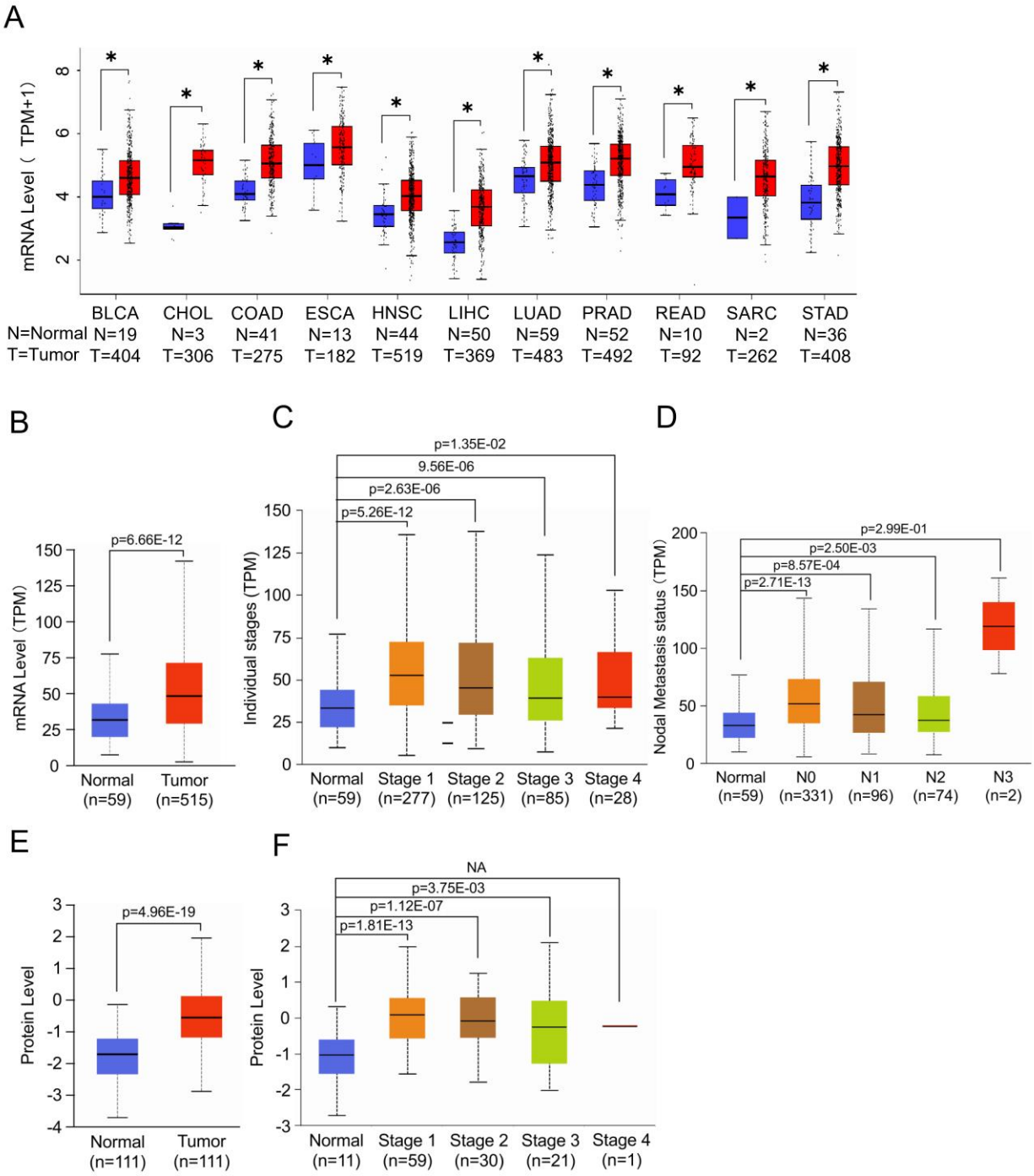

Supplemental Fig. 1 The expression pattern of OGT in TCGA and CTPAC databases.

A) Boxplot showing mRNA expression level of Ogt in multiple types of cancers. The plot was generated using the GEPIA2 online server. *p < 0.05. **B-D)** Boxplot showing mRNA expression level of *Ogt* in LUAD, Normal and tumor samples (**B**), Individual stages (**C**), Nodal metastasis

status (**D**). The plot was generated using the UALCAN online server. **E-F)** Boxplot showing protein expression level of OGT in LUAD, Normal and tumor samples (**E**), Individual stages (**F**). The plot was generated using the UALCAN online server (https://ualcan.path.uab.edu/analysis.html). Statistical significance was determined by Pearson test, unpaired Student's t-test, *$p < 0.05$, **$p < 0.01$, ***$p < 0.001$, ns, no significant difference. Data represent the mean of ± SD.

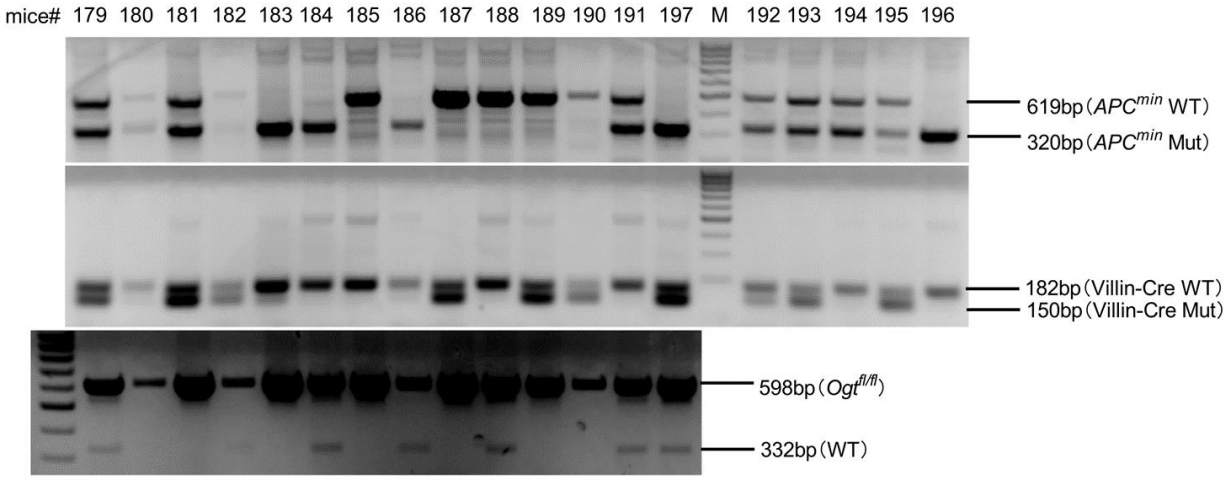

Supplemental Fig. 2. The genotype of *APC^{min}* ,*Villin-Cre* and *Ogt$^{fl/fl}$* mice.

Genomic DNA was extracted from the tails of *APC^{min}*, *Villin-Cre, and Ogt$^{fl/fl}$* mice and used for PCR with various primers. The resulting products were separated by agarose gel electrophoresis to determine the genotype.

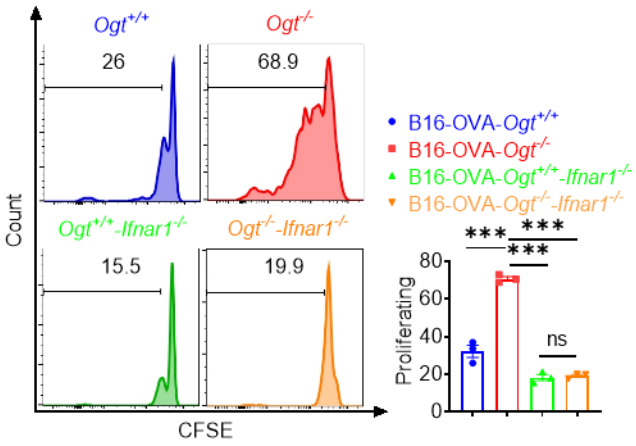

Supplemental Fig. 3 *In vitro* Cross-Priming of T Cells by *Ifnar*$^{-/-}$ BMDCs.

Ifnar1$^{-/-}$ BMDCs was pre-treated with B16-OVA-*Ogt*$^{+/+}$ or B16-OVA-*Ogt*$^{-/-}$ supernatant, and co-cultured with OT-1 T cell, then T cell proliferation was evaluated by flow cytometry. Representative fluorescence-activated cell sorting histograms and statistical data are shown. Data are representative of three independent experiments. Statistical significance was determined by one-way ANOVA, *p < 0.05, **p < 0.01, ***p < 0.001, ns, no significant difference. Data represent the mean of ± SD.

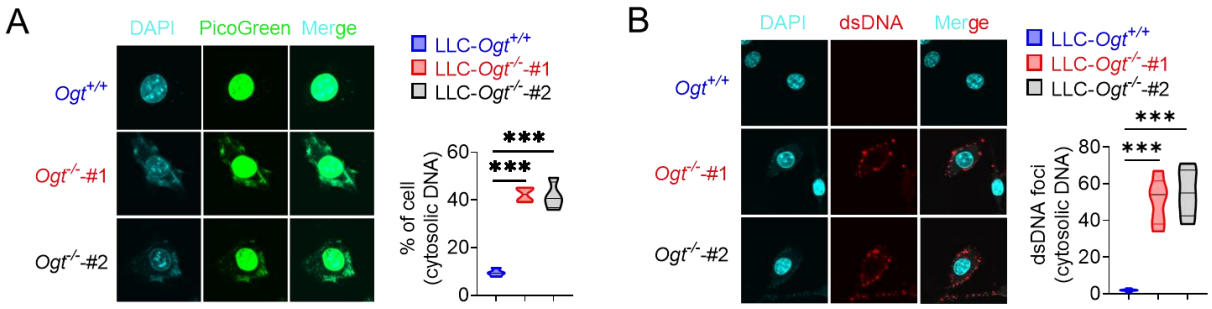

Supplemental Fig. 4 OGT deficiency causes DNA damage and accumulates cytosolic DNA. **A)** The extranuclear dsDNA in different *Ogt*$^{-/-}$ LLC clones were determined by PicoGreen staining assay and was quantified by image J. **B)** The extranuclear dsDNA in different *Ogt*$^{-/-}$ LLC clones were determined by anti-dsDNA fluorescence staining assay and was quantified by image J. Data are representative of three independent experiments. Statistical significance was determined by unpaired Student's t-test, two-way ANOVA, *$p < 0.05$, **$p < 0.01$, ***$p < 0.001$, ns, no significant difference. Data represent the mean of ± SD.

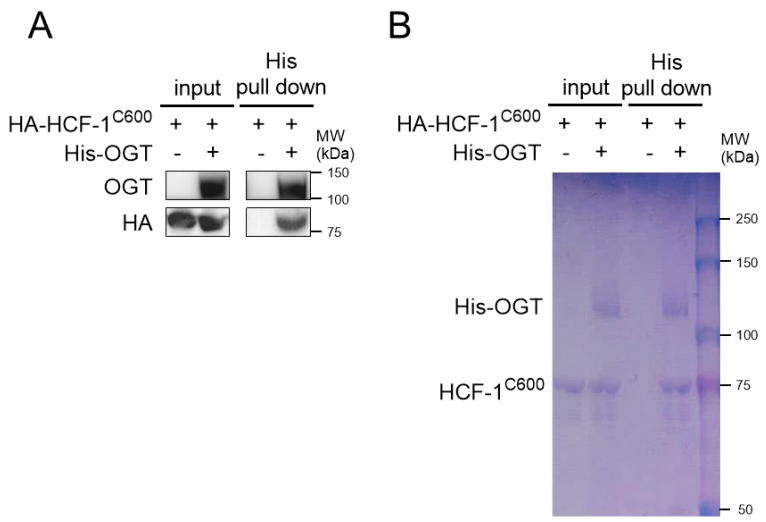

Supplemental Fig. 5 *In vitro* pull-down assay analysis of the interaction of HCF-1^{C600} and OGT.

A) His pull-down assays were used to analyze the interaction between HCF-1C600 and OGT. **B)** His-tagged OGT and HCF1 were expressed and purified, followed by SDS-PAGE separation and staining with Coomassie blue.

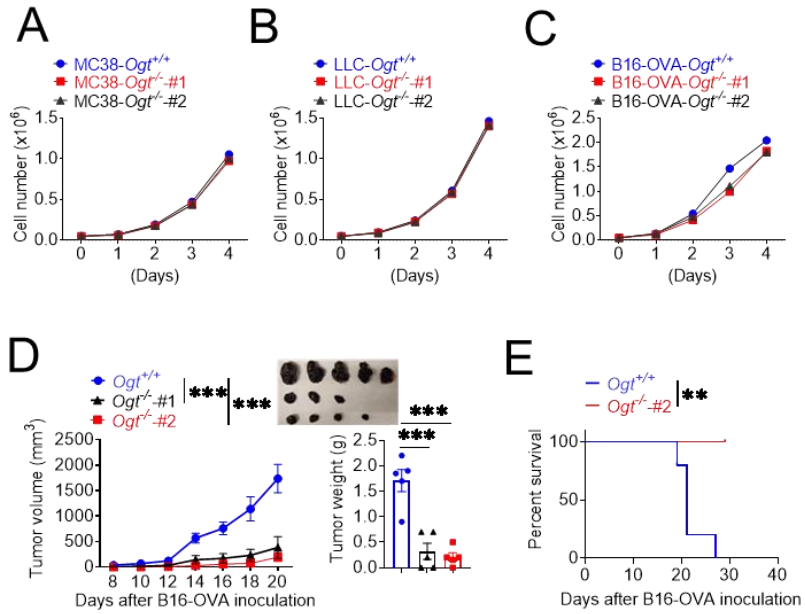

Supplemental Fig. 6 The cell proliferation of different tumor model *in vitro* and B16-OVA tumor growth analysis *in vivo*.

A-C), The cell proliferation of different $Ogt^{-/-}$ tumor model in vitro. **A)** MC38, **B)** LLC, **C)** B16-OVA $Ogt^{-/-}$ cells proliferation in *vitro*. **D-E)** Tumor volume, weight of $Ogt^{+/+}$ or $Ogt^{-/-}$ B16-OVA tumors in C57BL/6J mice, and mice survival, n=5 respectively. Data are representative of two or three independent experiments. Statistical significance was determined by unpaired Student's t-test, two-way ANOVA, $*p < 0.05$, $**p < 0.01$, $***p < 0.001$, ns, no significant difference. Data represent the mean of ± SD.

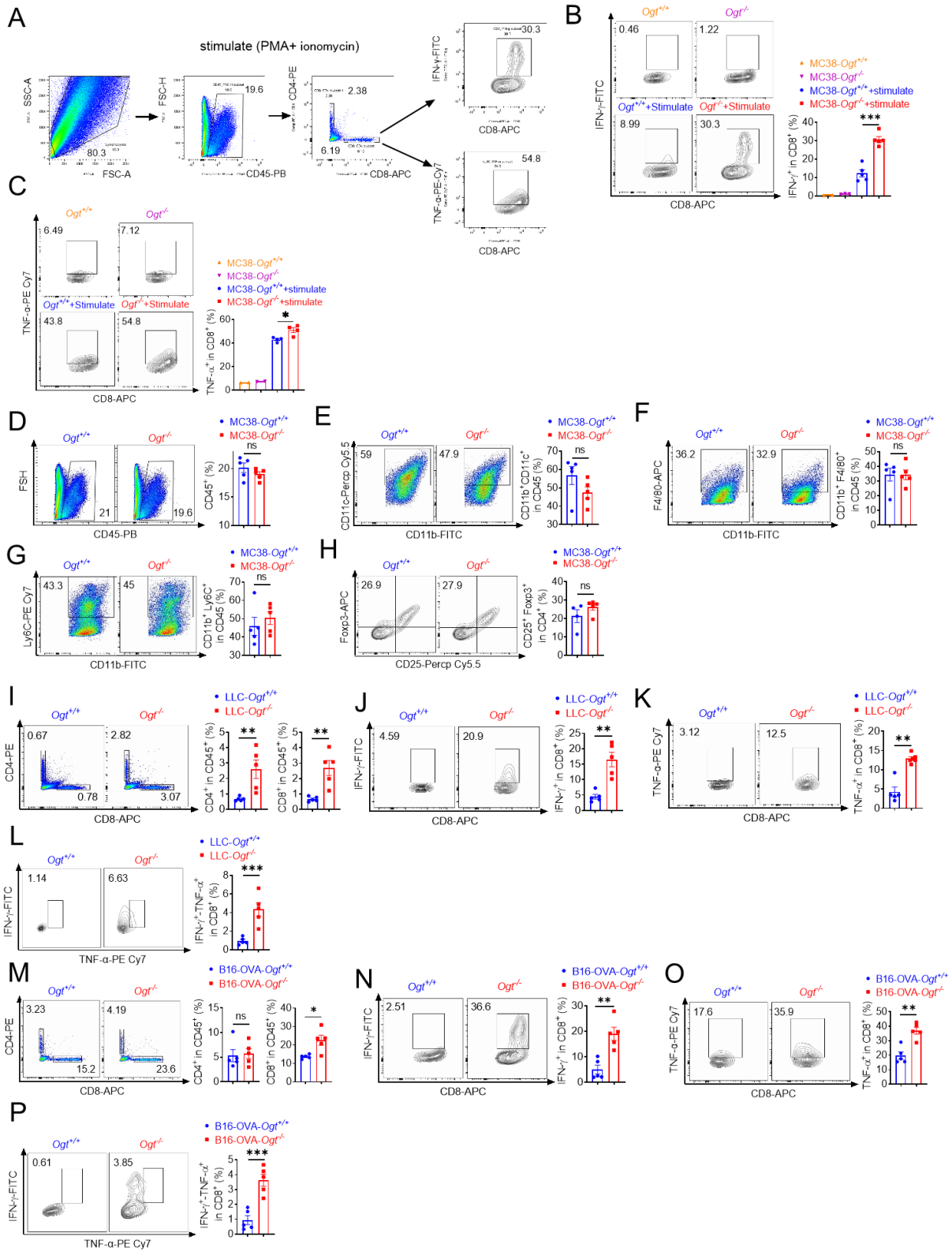

Supplemental Fig. 7 *Ogt* deficiency inhibits tumor progression through enhancing infiltration of CD8$^+$ T cells.

A) A total schematic of flow cytometry analysis. **B-C)** Flow cytometry analysis showing percentage of IFN-γ and TNF-α-expressing intratumoral CD8$^+$ T cells in MC38 tumors with or without PMA and ionomycin stimulation. **D-H)** Flow cytometry analysis showing percentage of CD45$^+$ (**D**), CD11b$^+$ CD11c$^+$ (**E**), CD11b$^+$ F4/80$^+$ (**F**), CD11b$^+$ Ly6C$^+$ (**G**) and Treg cells (**H**) in MC38 tumor model, n=5 respectively. **I-P)** Flow cytometry analysis showing percentage of CD4$^+$ and CD8$^+$ T cells in LLC (**I**), B16-OVA cells (**M**). IFN-γ$^+$, TNF-α$^+$ and IFN-γ$^+$ TNF-α$^+$ double positive expressing intratumoral CD8$^+$ T cells in LLC (**J-L**), or B16-OVA (**N-P**) tumors isolated at day 18 post-tumor inoculation, n=5 respectively. Data are representative of two or three independent experiments. Statistical significance was determined by unpaired Student's t-test, one-way ANOVA, *p < 0.05, **p < 0.01, ***p < 0.001, ns, no significant difference. Data represent the mean of ± SD.

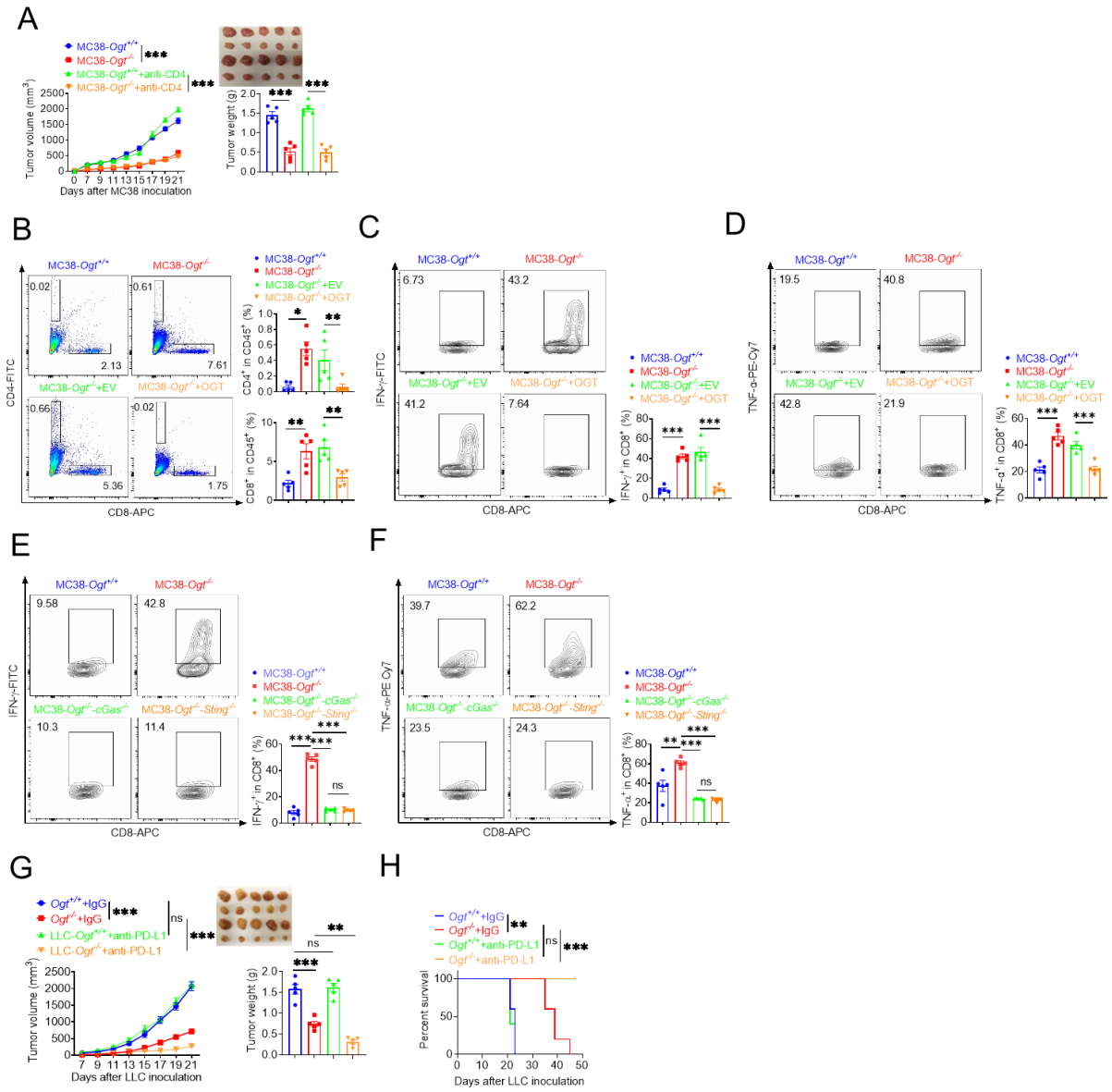

Supplemental Fig. 8. *Ogt* deficiency inhibits tumor progression through enhancing infiltration of CD8$^+$ T cells.

A) Tumor volume and weight of *Ogt*$^{+/+}$ or *Ogt*$^{-/-}$ MC38 tumors injected with control IgG or anti-CD4 antibody at day 0, 7 and 14 post tumor inoculation in C57BL/6J mice, n=5 respectively. **B-D)** The percentage of CD4$^+$ and CD8$^+$ T cells (**B**), CD8$^+$ IFN-γ$^+$ (**C**) and CD8$^+$ TNF-α$^+$ (**D**) in *Ogt*$^{-/-}$ rescued MC38 tumors isolated at day 18 post-tumor inoculation. **E-F**) Flow cytometry analysis

showing percentage of $CD8^+$ IFN-γ (**E**), $CD8^+$ TNF-α^+ (**F**) in *Ogt*$^{-/-}$*cGAS*$^{-/-}$ or *Ogt*$^{-/-}$*Sting*$^{-/-}$ double knockout MC38 tumors in C57BL/6J mice, subcutaneous tumor isolated at day 18 post-tumor inoculation. **G-H)** Tumor volume, weight of *Ogt*$^{+/+}$ or *Ogt*$^{-/-}$ LLC tumors injected with control IgG or anti-PD-L1 antibody at day 7, 10 and 13 post tumor inoculation in C57BL/6J mice, and mice survival, n=5 respectively. Data are representative of two or three experiments. Statistical significance was determined by unpaired Student's t-test, one-way ANOVA, two-way ANOVA, $*p < 0.05$, $**p < 0.01$, $***p < 0.001$, ns, no significant difference. Data represent the mean of ± SD.

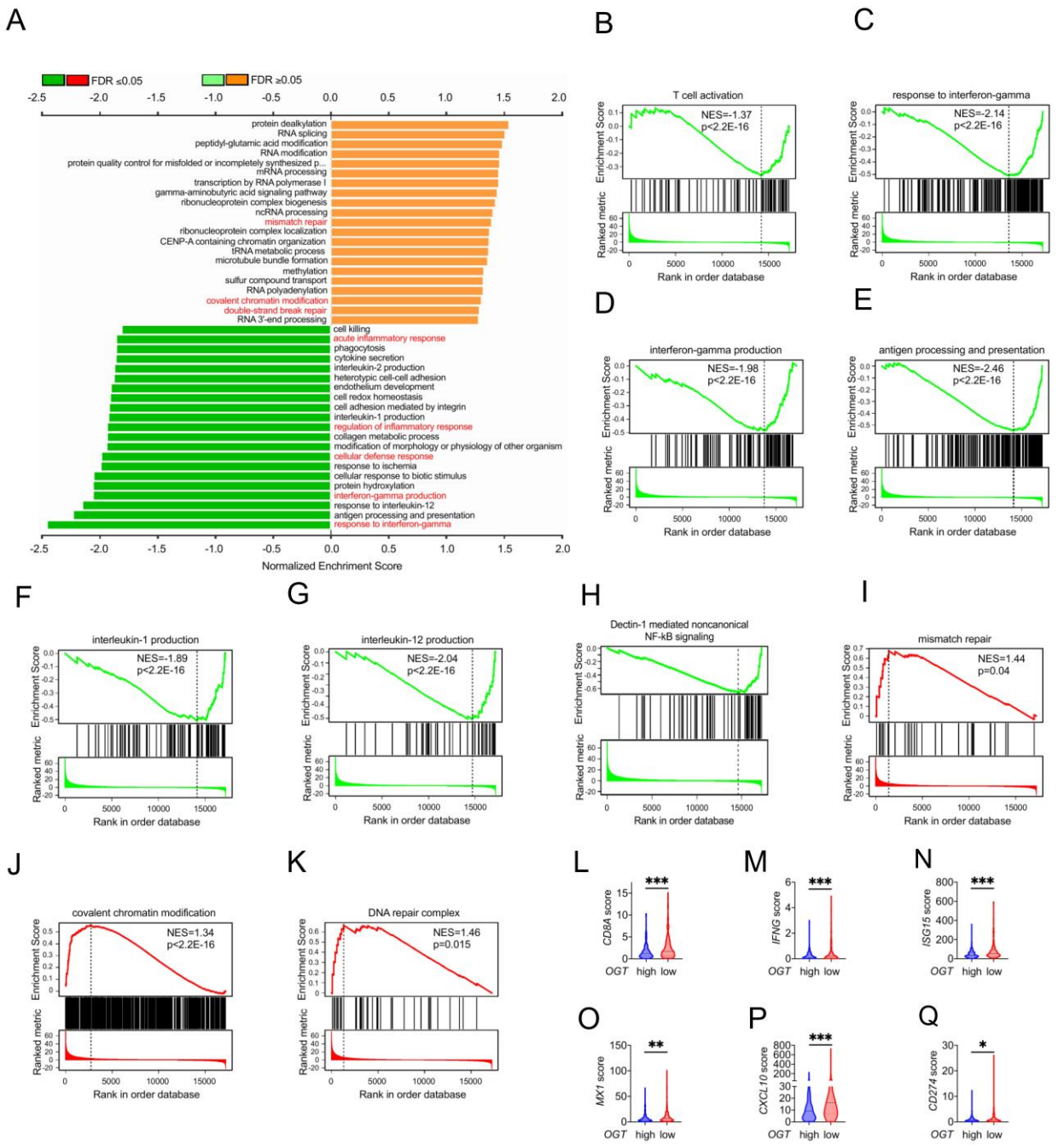

Supplemental Fig. 9 *OGT* expression is negatively related to CD8$^+$ T cells infiltration in human colorectal cancer.

A) Gene Ontology (GO) enrichment and pathway analysis in *OGT* high and *OGT* low patients. **B-K)** GSEA analysis in *OGT* high and *OGT* low patients. T cells activation (**B**), response to interferon-gamma (**C**), interferon-gamma production (**D**), antigen processing and presentation (**E**),

interleukin-1 production (**F**), interleukin-12 production (**G**), dectin-1 mediated noncanonical NF-κB signaling (**H**), mismatch repair (**I**), covalent chromatin modification (**J**) and DNA repair complex (**K**) in *OGT* high and *OGT* low patients. **L-Q)** RNAseq analysis of mRNA expression pattern in *OGT* high and *OGT* low patients, CD8A (**L**), *IFNG* (**M**), *ISG15* (**N**), *MX1* (**O**), *CD274* (**P**) and *CXCL10* (**Q**) mRNA expression patterns in *OGT* high and *OGT* low patients. Statistical significance was determined by Pearson test, unpaired Student's t-test, $*p < 0.05$, $**p < 0.01$, $***p < 0.001$, ns, no significant difference. Data represent the mean of ± SD.

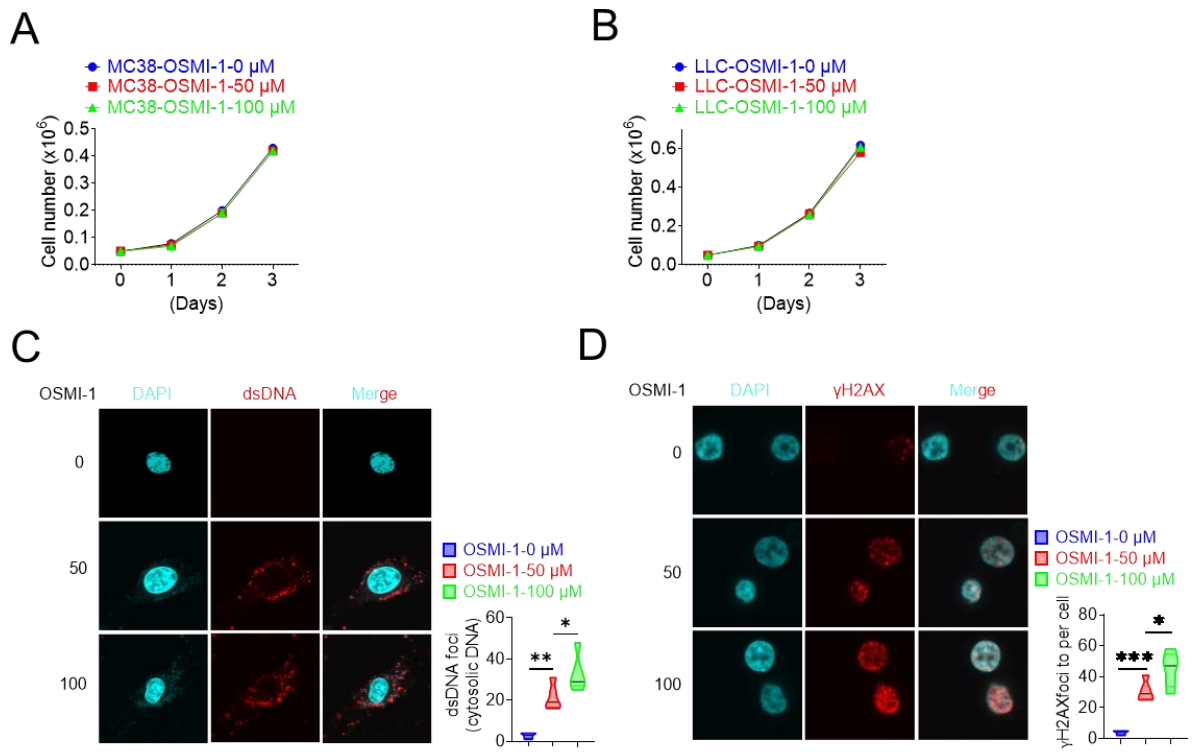

Supplemental Fig. 10 OSMI-1 could significantly induce a high percentage of DNA damage. **A-B)** The cell proliferation in different treatments in *vitro*. **A)** MC38 cell proliferation, **B)** LLC cell proliferation. **C)** The extranuclear dsDNA was measured by anti-dsDNA fluorescence staining treated with 50 μM and 100 μM in LLC cells, respectively. **D)** The γH2AX expression was measured anti-γH2AX fluorescence staining treated with 50 μM and 100 μM in LLC cells, respectively. Data are representative of three experiments. Statistical significance was determined by one-way ANOVA, $*p < 0.05$, $**p < 0.01$, $***p < 0.001$, ns, no significant difference. Data represent the mean of ± SD.

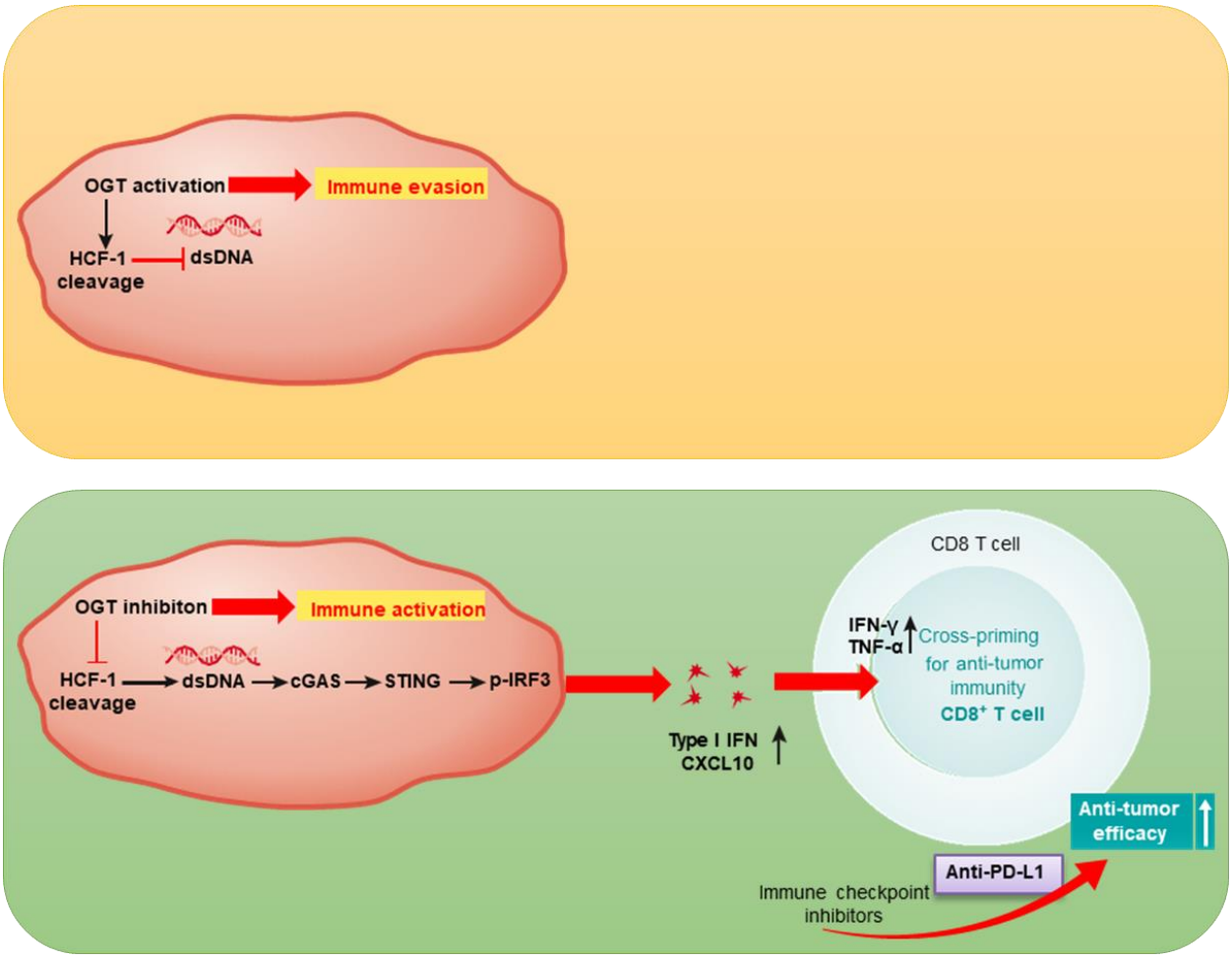

Supplementary Fig. 11 A schematic of critical role of OGT-mediated antitumor immunity.

Inhibition of O-GlcNAc transferase promotes the activation of cGAS-STING pathway and the production of type I interferon, which enhances CD8 T cells dependent antitumor immunity.

Table S1. Primer sequences for genotype

Genes	Sequence	Size
Ogt$^{fl/fl}$	Forward CATCTCTCCAGCCCCACAAACTG	WT 332 bp,
	Reverse GACGAAGCAGGAGGGGAGAGCAC	Mutant 487 bp
Villin-Cre	WT Forward TATAGGGCAGAGCTGGAGGA	WT 182 bp,
(*⊿IEC*)	Mut Forward AGGCAAATTTTGGTGTACGG	Mutant 150 bp
	Common Rev GCCTTCTCCTCTAGGCTCGT	
Apc^{min}	WT Forward GCCATCCCTTCACGTTAG	WT 619 bp,
	Mut Forward TTCTGAGAAAGACAGAAGTTA	Mutant 320 bp
	Common Rev TTCCACTTTGGCATAAGGC	

Table S2. Related to Experimental Procedures. Primer sequences for RT-PCR

Genes	Forward	Reverse
Mouse *Ifna4*	CCTGTGTGATGCAGGAACC	TCACCTCCCAGGCACAGA
Mouse *Ifnb1*	ATGAGTGGTGGTTGCAGGC	TGACCTTTCAAATGCAGTAGAGTCA
Mouse *Ifng*	TCAAGTGGCATAGATGTGGAAGAA	TGGCTCTGCAGGATTTTCATG
Mouse *Il1a*	GCACCTTACACCTACCAGAGT	AAACTTCTGCCTGACGAGCTT
Mouse *Il1b*	CTCATTGTGGCTGTGGAGAAG	ACCAGCAGGTTATCATCATCAT
Mouse *Il6*	AGCTGGAGTCACAGAAGGAG	AGGCATAACGCACTAGGTTT
Mouse *Il10*	CCCTTTGCTATGGTGTCCTT	TGGTTTCTCTTCCCAAGACC
Mouse *Il12a*	GAGGACTTGAAGATGTACCAG	TCCTATCTGTGTGAGGAGGGC
Mouse *Tnfa*	GTCAGGTTGCCTCTGTCTCA	TCAGGGAAGAGTCTGGAAAG
Mouse *Cxcl10*	CCTGCCCACGTGTTGAGAT	TGATGGTCTTAGATTCCGGATTC
Mouse *Isg15*	TGGAAAGGGTAAGACCGTCCT	GGTGTCCGTGACTAACTCCAT
Mouse *Mx1*	GGGGAGGAAATAGAGAAAATGAT	GTTTACAAAGGGCTTGCTTGCT
Mouse *Actb*	AGGGCTATGCTCTCCCTCAC	CTCTCAGCTGTGGTGGTGAA
Human *IFNB1*	CATTACCTGAAGGCCAAGGA	CAATTGTCCAGTCCCAGAGG
Human *ISG15*	CTGAGAGGCAGCGAACTCAT	AGCATCTTCACCGTCAGGTC
Human *MX1*	AGAGAAGGTGAGAAGCTGATCC	TTCTTCCAGCTCCTTCTCCTG
Human *CXCL10*	CTCCAGTCTCAGCACCATGA	GCTCCCCTCTGGTTTTAAGG
Human *GADPH*	ATGACATCAAGAAGGTGGTG	CATACCAGGAAATGAGCTTG

Table S3. Related to CRISPR/Cas9. Primer sequences for molecular cloning

Genes	Forward	Reverse
Ogt gRNA#1	CACCGTGCCCACGGAAGACGCCATC	AAACGATGGCGTCTTCCGTGGGCAC
Ogt gRNA#2	CACCGGCTCCAGATGGCGTCTTCCG	AAACCGGAAGACGCCATCTGGAGCC
mMavs gRNA#1	ACCGGCCGTCGCGAGGATGTCTGG	AACCCAGACATCCTCGCGACGGCC
mMavs gRNA#2	CACCGGATACCCTCTCCTAACCAGC	AACGCTGGTTAGGAGAGGGTATCC
mCgas gRNA	CACCGATATGGAAGATCCGCGTAGA	AAACTCTACGCGGATCTTCCATATC
mSting gRNA	CACCGGCTGGATGCAGGTTGGAGTA	AAACTACTCCAACCTGCATCCAGCC
hcGAS gRNA	CACCGAAGTGCGACTCCGCGTTCAG	AAACCTGAACGCGGAGTCGCACTT
hSTING gRNA	CACCGGGATGTTCAGTGCCTGCGAG	AAACCTCGCAGGCACTGAACATCC

Table S4. Mass spectrometry assay of OGT interactome